JGR Space Physics

RESEARCH ARTICLE
10.1029/2025JA034034

Formation Mechanism and Interhemispheric Asymmetry of Storm-Enhanced Density During April 2023 Storm Revealed by GITM

Yulu Peng[1], Shasha Zou[1], Zihan Wang[2], Xiantong Wang[1], Aaron Ridley[1], Grace Kwon[1], and Mary Smirnova[1]

[1]Department of Climate and Space Sciences and Engineering, University of Michigan, Ann Arbor, MI, USA, [2]Department of Physics, University of Texas at Arlington, Arlington, TX, USA

Key Points:

- Two periods of Storm-Enhanced Density (SED) with opposite hemispheric asymmetries during the 23 April 2023 storm were studied
- Equatorward winds dominated the SED plasma lifting in midlatitudes and convection electric field dominated above subauroral latitudes
- Complex thermospheric composition change and its time history played a critical role in determining the SED location and morphology

Supporting Information:

Supporting Information may be found in the online version of this article.

Correspondence to:

Y. Peng,
yulupeng@umich.edu

Citation:

Peng, Y., Zou, S., Wang, Z., Wang, X., Ridley, A., Kwon, G., & Smirnova, M. (2025). Formation mechanism and interhemispheric asymmetry of storm-enhanced density during April 2023 storm revealed by GITM. *Journal of Geophysical Research: Space Physics*, *130*, e2025JA034034. https://doi.org/10.1029/2025JA034034

Received 1 APR 2025
Accepted 9 SEP 2025

© 2025. The Author(s).
This is an open access article under the terms of the Creative Commons Attribution License, which permits use, distribution and reproduction in any medium, provided the original work is properly cited.

Abstract We investigate the formation and interhemispheric asymmetries of storm-enhanced density (SED) during the April 23–24, 2023 geomagnetic storm using the Global Ionosphere-Thermosphere Model (GITM) coupled with high-latitude drivers from the Geospace model. This storm, driven by an interplanetary coronal mass ejection (ICME), featured two southward IMF intervals—the ICME sheath followed by a magnetic cloud (MC)—each producing SED with distinct asymmetries. During the sheath phase, SEDs formed in both hemispheres with a stronger isolated peak in the south. During the MC phase, a weaker SED appeared only in the north, despite a stronger IMF B_z. GITM results indicate that equatorward neutral wind-induced upward ion drift was the primary driver of midlatitude SEDs, while convection electric fields dominated high-latitude SED and plume lifting. Differences in SED response between the two phases highlight the role of thermospheric composition and its temporal history in shaping storm-time ionospheric density, including pre-storm modulation, storm-time reinforcement, and interhemispheric asymmetry of magnetic poles with universal time (UT) effect. The prominent southern SED during the sheath phase was attributed to a higher O/N2 ratio from preconditioning and storm-time reinforcement, whereas the expanded convection during the MC phase lowered O/N2 in southern midlatitudes and limited SED growth. The impacts of large-scale traveling atmospheric/ionospheric disturbances (TADs/TIDs) on SED formation were minimal. This study quantifies various factors driving SED formation and highlights the sustained impact of ICME sheath during a double-dip storm on ionosphere-thermosphere dynamics and the role of thermospheric composition in modulating SED location, characteristics, and hemispheric asymmetry.

1. Introduction

During geomagnetic storms, large-scale energy and momentum exchanges occur between the solar wind and the Earth's geospace environment. Part of the solar wind energy entering the magnetosphere deposits into the ionosphere-thermosphere (IT) system and manifests as enhanced convection electric fields and field-aligned currents (FACs). These energy input variations cause significant IT perturbations, including ionospheric storms (Buonsanto, 1999). Ionospheric storms refer to substantial changes in the ionospheric electron density or total electron content (TEC) during geomagnetic storms. Such variations in density or TEC structures are often accompanied by large density gradients, which can affect radio signal propagation, and thus disrupt modern navigation and communication systems (Coster & Foster, 2007; Doherty et al., 2004; Wernik et al., 2003). Consequently, characterizing and understanding the formation mechanisms of ionospheric density structures and their evolution is crucial in space weather research.

Since the ionosphere is electromagnetically coupled to the solar wind-magnetosphere and collisionally coupled to the thermosphere, its responses during storms are complex and exhibit strong latitudinal and longitudinal dependencies and spatial variations (Coster & Foster, 2007; Mendillo, 2006; Prölss, 1993a). Historically, ionospheric storms have been separated into two phases, that is, an initial positive stage and a following negative stage. The ionospheric positive storms refer to the initial periods of increased density/TEC during geomagnetic storms, and negative storms are vice versa. However, the sequences, durations, and locations of positive or negative phases can vary between cases (Liu et al., 2010; Lu et al., 2001; Mannucci et al., 2009). For decades, the community has focused on a key feature associated with ionospheric storms: storm-enhanced density (SED), a distinct region of high electron density with an elevated F-region peak height (hmF2) in the dayside midlatitude region (Buonsanto, 1995a, 1995b; Foster et al., 2021; Heelis, 2016; Mannucci et al., 2005; Mendillo et al., 1972;

Tsurutani et al., 2004). Another common accompanying feature is the SED plume, a latitudinally narrow enhancement streaming in the subauroral plasma flow that may be replenished from the SED base plasma (Foster, 1993; Foster et al., 2021).

During active times, both low- and high-latitude ionospheric dynamic systems expand and thus the midlatitude region becomes a site of complex interplay among various drivers, including prompt penetration electric fields (PPEF), shielding electric fields, disturbance dynamo electric fields (DDEF), neutral winds and neutral compositions. The influence of these drivers on the ionosphere varies spatially and temporally, particularly in relation to the SED generation (Blanc & Richmond, 1980; Erickson et al., 2010; Fuller-Rowell et al., 1994; Lu et al., 2014; Schunk & Nagy, 2000; Zou et al., 2013, 2014). For example, the PPEF can quickly reach low-midlatitudes right after the southward interplanetary magnetic field (IMF) conditions. Zou and Ridley (2016) demonstrated the rapid responses of the altitude profiles of SED plasma to PPEF variations after southward and northward IMF turnings using the Global Ionosphere Thermosphere Model (GITM). The duration of PPEF depends on the time scale of establishing shielding in the inner magnetosphere, which is associated with the ring current development and ionospheric conductivity (Fejer et al., 1990; Sazykin, 2000; Wolf, 1983). Meanwhile, the disturbance winds create the DDEF through a dynamo process (Lu et al., 2012; Maruyama et al., 2005), which later enters the competition among these electric fields. The net electric field resulting from these interplays may facilitate the generation of SED by providing upward E × B drift (Heelis et al., 2009; Zou et al., 2013, 2014).

In addition, meridional neutral winds and the expansion of equatorial ionization anomaly (EIA) have also been reported as contributors to the SED formation (Anderson, 1976; Kelley et al., 2004; Tsurutani et al., 2004; Zou et al., 2014). Equatorward directed neutral winds from the auroral zone push plasma upward along the magnetic field lines, lifting the plasma to higher altitudes. At higher altitudes, where the recombination rates are lower, the ionospheric plasma has a longer lifetime. With continued production due to the solar EUV radiation, the density within the SED can increase. Therefore, both the E × B drift and the equatorward wind play roles in explaining the higher F-region peak and increased TEC within the SED. Zou et al. (2014) highlighted the variability within the SED and the associated SED plumes across six storms, emphasizing the diverse combinations of electric fields and winds that contributed to the density and TEC meso-scale structures within the SED. Lu et al. (2012) used TIMEGCM to study the 2-hr PPEF event, during which the disturbance meridional winds produced by the high-latitude Joule heating competed with the vertically directed E × B drifts in the midlatitude regions. Additionally, in the high latitudes, the enhanced Joule and particle heating not only drive large-scale thermospheric wind circulation changes but also alter the thermospheric composition (O/N_2), which affects the plasma lifetime by changing the charge exchange and recombination rates (Crowley et al., 2006; Forbes, 2007; Meier et al., 2005). Changes in the thermospheric composition are often invoked to explain the negative ionospheric storm phase.

The IT system exhibits interhemispheric asymmetries (IHA) in many physical parameters, such as the ionospheric density and TEC. One of the determining factors of the IT IHA is the seasonal effect. The distribution of the solar EUV radiation varies seasonally and generates differences in neutral temperature and mass density, leading to the seasonal variations in large-scale neutral wind circulation (Dhadly et al., 2017; Qian et al., 2016; Sutton et al., 2009). The seasonal asymmetries in the ionospheric conductance and FACs at high latitudes also affect the energy deposition asymmetry and consequently lead to asymmetries in the neutral wind circulation at high latitudes (Ridley, 2007; Workayehu et al., 2020; Zhu et al., 2022).

Hemispheric differences in the auroral zone energy input also result in the variations in ion drift, neutral wind and density, which further generate asymmetries in large-scale traveling ionospheric disturbance (TID), traveling atmospheric disturbance (TAD) and the O/N_2 ratios (Eriksson et al., 2002; Förster et al., 2008; Grocott & Milan, 2014; Terefe et al., 2024; Yu et al., 2023; Zhu et al., 2023). Various satellite observations confirm the importance of the IMF B_y component on hemispheric energy input differences: the south hemisphere (SH) receives more energy than the north hemisphere (NH) under predominately positive B_y conditions and vice versa; and generally, the NH experiences greater energy input even during the equinox (Knipp et al., 2021; Liou et al., 2001; Oliveira & Zesta, 2024; Pakhotin et al., 2021). Using simulations, Hong et al. (2023) revealed that energy input was asymmetric between the two hemispheres when the IMF By dominated, which led to asymmetric neutral densities.

In addition, extensive modeling efforts also show that the IT IHA originates from the magnetic pole offset and universal time (UT) dependence. Because the southern hemisphere has a larger offset, it has stronger UT variations and greater enhancements in plasma density and thermospheric heating (Liu et al., 2017; Perlongo &

Ridley, 2016). Finally, forcing and eddy diffusion from the lower atmosphere also contribute to the asymmetry, primarily at low latitudes during quiet times (Conte et al., 2017; Hagan & Forbes, 2003; Qin et al., 2019).

Consequently, the hemispheric asymmetry of SEDs at middle latitudes is the net outcome of these multiple contributors (Astafyeva et al., 2020; Lin et al., 2022; Yue et al., 2016). For example, Wang et al. (2021) studied two episodes of asymmetric SEDs during the September 2017 storm and attributed the SED asymmetry to the storm-time changes in thermospheric composition that reinforced the seasonal asymmetry. For the November 2021 storm, it was found that changes in the thermospheric composition and PPEF calculated by a real-time forecast model contributed more significantly to the ionospheric positive phase in the northern hemisphere across all longitude sectors (Aol et al., 2024). Studying two solstice storms in June and December 2015, Kalita et al. (2024) found that ionospheric TEC responses were hemispherically symmetric during the main phase but became asymmetric during the recovery phase. Furthermore, this asymmetry was opposite to the quiet-time TEC asymmetry due to seasonal effect (Kalita et al., 2022).

In this paper, the ionospheric responses are examined during the April 23–24, 2023, a double-dip storm. Section 2 describes the GITM simulation inputs and setup. The solar wind and IMF conditions during the storm are discussed in Section 3. In Section 4, we present the simulation results, focusing on two periods of SEDs following the southward B_z turnings: ∼16-22UT April 23rd (ICME sheath) and ∼01–09 UT April 24th (ICME magnetic cloud). During the first period, the hemispheric asymmetry of the SED developed with the dominant one in the southern hemisphere. In the second period, the SED asymmetry reversed with a relatively stronger northern SED, while the overall dayside ionospheric TEC became weaker. The key factors, that is, ion upward drifts driven by different factors, and the potential role of TIDs/TADs are also examined. Comparisons between model and observation are presented at the end of Section 4. At the end, we discuss and conclude the formation mechanisms for the SEDs and their asymmetries during these two periods.

2. Model Description and Simulation Setup

GITM is a three-dimensional spherical model that self-consistently simulates the Earth's thermosphere and ionosphere system with an adjustable grid (Ridley et al., 2006). GITM solves the coupled continuity, momentum, and energy equations for 7 neutral and 7 ion species. In this study, the spatial resolution of the GITM is set to 2° in latitude and longitude. The high-latitude electric fields, auroral particle precipitation, and solar radiations are user-defined model inputs. Flare Irradiance Spectral Model 2 (FISM2), an empirical model of solar irradiance spectrum from 0.01 to 190 nm at 0.1 nm spectral bins (Chamberlin et al., 2020), provides solar irradiance input.

For the April 2023 storm study, we first used the empirical Weimer (2005) model as the high-latitude convection driver and the Fuller-Rowell-Evans auroral model (Fuller-Rowell & Evans, 1987) as auroral particle heating for steady state initialization on April 22nd. In the following 2-day time accurate run of the storm, we used the Ionospheric Electrodynamic output (IE) from the Space Weather Modeling Framework (SWMF) Geospace suite (e.g., Gombosi et al., 2021; Tóth et al., 2005; Wang et al., 2019). The SWMF Geospace suite includes three components: the Global Magnetosphere (GM), the Inner-Magnetosphere (IM) (simulated by the Rice Convection Model, RCM), and the Ionospheric Electrodynamics (IE) (simulated by the Ridley Ionosphere Model, RIM). The GM component uses the BATS-R-US (Block-Adaptive-Tree-Solarwind-Roe-Upwind-Scheme) MHD model to provide the numerical solution of the global magnetosphere. The pressure and density solution of BATS-R-US grid cells connected to the RCM boundary are adjusted toward the RCM solution (De Zeeuw et al., 2004), which contributed to a more accurate ring current and Region-2 FAC solution in the inner magnetosphere (Toffoletto et al., 2003). The electric field calculated by RIM is mapped back to BATS-R-US for its inner-boundary condition, and the electric potential is also sent to RCM to advect the field lines. Traditionally, the Ridley Legacy Model (RLM, Ridley et al., 2004) has been used to derive the ionospheric conductance model in the RIM. Comparing the simulated D_{st} index with observations, we found that the runs using the new COMPASS conductance model (Wang & Zou, 2022) performed better. Therefore, the IT responses during this storm event were simulated by GITM driven by the IE outputs from the SWMF Geospace suite and the ionospheric conductance model in the IE module was based on the COMPASS model.

3. Solar Wind and IMF Driver Conditions

Figure 1 illustrates the April 2023 storm external driver conditions, including the IMF By and B_z components, solar wind speed, density, and the observed and simulated SYM-H indices. A coronal mass ejection (CME)

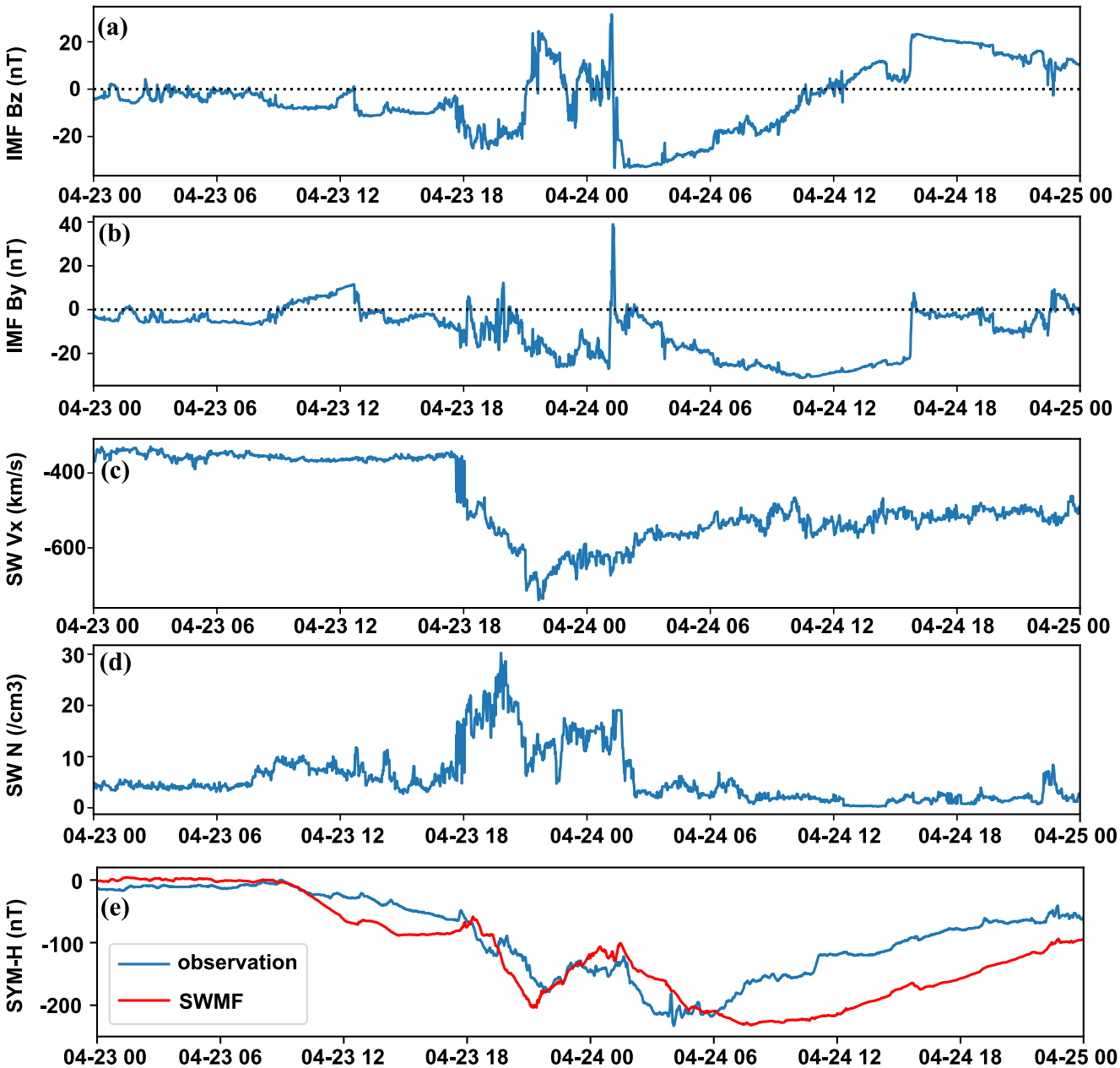


Figure 1. Geospace conditions during 22–25 April 2023 storm. (a, b) Interplanetary magnetic field B_z and B_y, (c) solar wind speed, (d) solar wind density, and (e) observed (blue) and simulated (red) SYM-H index.

initiated on the Sun on April 21st and arrived at the Earth at 17:37 UT on April 23rd, leading to an intense double-dip geomagnetic storm (Ghag et al., 2024). On April 23rd, the solar wind speed suddenly increased from ∼350 km/s to ∼700 km/s at ∼17:37 UT, signaling the ICME shock arrival. During the ICME sheath impact, the IMF B_z remained southward from ∼18 to 21 UT with a minimum value of −21 nT, which led to the first dip in SYM-H. The IMF B_z turned northward at ∼21 UT on April 23rd and was mainly northward until ∼01:40 UT on April 24th. Meanwhile, the B_y component was mainly negative and fluctuated around −20 nT. The storm continued through April 24th with a clear feature of magnetic cloud in the IMF data. During the magnetic cloud, the B_z reached a minimum value of −33 nT at ∼01:30 UT and remained southward until ∼11 UT, while the B_y was strongly negative and exceeded −30 nT toward the end of the cloud period at ∼16 UT on April 24th. The SYM-H index with 1-min resolution reached the first dip of −179 nT at 22 UT on April 23rd, and the minimum

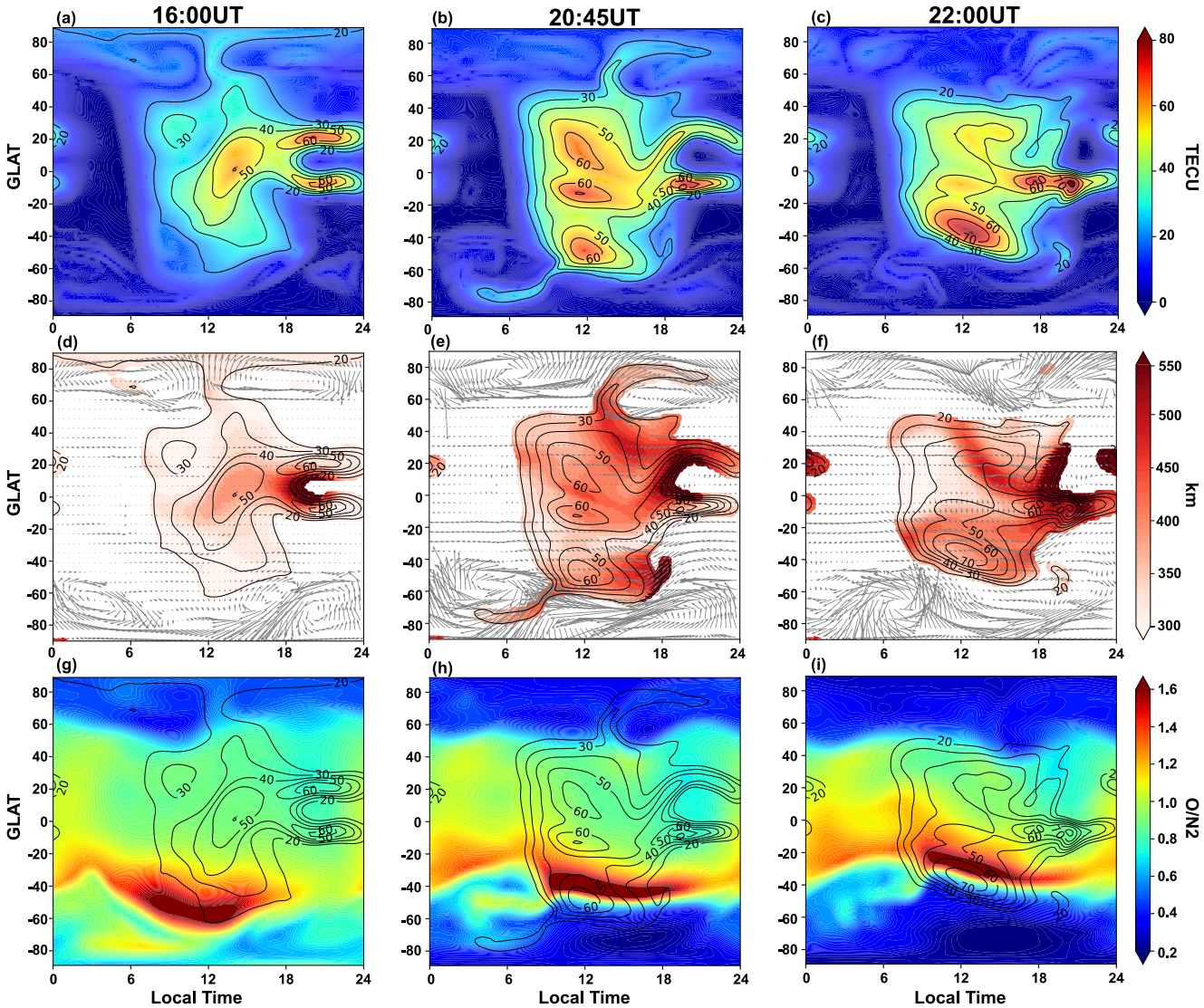


Figure 2. Formation and evolution of the first SED base and plume during the first ICME sheath southward IMF period revealed by GITM. (a–c) Global TEC map with TEC contour lines, (d–f) color contours of hmF2 in regions with TEC greater than 20 TECU; TEC contour lines and ion velocity vectors are also plotted, (g–i) $\Sigma O/N_2$ ratio with TEC contour lines.

value of −233 nT at ∼04 UT on April 24th, followed by a long storm recovery phase. Figure 1e also shows that the simulated SYM-H index from the SWMF Geospace suite reproduces the observed double-dip features.

4. Results

4.1. SED During the First Southward IMF Period

Figure 2 shows the formation and evolution of SED and its asymmetry during the first southward B_z period from GITM. Three time cadences are selected to show the SED conditions before the storm, during the first southward B_z period, and shortly after the northward turning. The first row shows the TEC map with contours, the second row indicates the hmF2 for the regions with TEC greater than 20 TECU, which are selected to highlight the dayside SED features, and the third row presents the height-integrated $\Sigma O/N_2$ ratio. The $\Sigma O/N_2$ ratio from GITM is height-integrated from the upper boundary of the model until the integral of N_2 reaches 10^{21} particles/m^2, similar to the $\Sigma O/N_2$ ratio based on observations (Meier et al., 2005). The TEC contour lines from the first row are also superimposed onto the second and third rows for easy comparison. A Movie S1 of the same format as Figure 2 is provided as Supporting Information for this paper.

At 16 UT, before the storm, the ionosphere was relatively quiet, with the TEC reaching ∼50 TECU near the dayside equator. The hmF2 near the noon equator was at ∼370 km, and the remnant of EIA near the dusk terminator was lifted to more than 500 km due to the pre-reversal enhancement (PRE). The $\Sigma O/N_2$ ratio showed the typical seasonal asymmetry with higher values in the winter hemisphere, that is, the southern hemisphere in this case. There was some density increase and a plume in the northern hemisphere due to the weakly southward IMF B_z even before the ICME arrival.

At 20:45 UT, ∼3 hr after the IMF southward turning, the EIA around noon bifurcated with the two crests centered at +20° and −10° geographic latitudes and an averaged hmF2 of ∼400 km, indicating the enhanced fountain effect due to PPEF during the southward IMF. SED plumes developed at high-latitude regions in both hemispheres. In the midlatitude regions, the SED base clearly developed in both hemispheres and with significant asymmetries. The northern SED base is connected to the plume at ∼14 LT with an average of ∼35 TECU and is smoothly connected to the northern EIA. In the south hemisphere, the SED base clearly shows a separate peak from the southern EIA. The southern SED base covered a large area ranging from −40° to −60° latitude and across 10–16 LT over the Pacific Ocean, and the peak TEC within this SED base exceeded ∼60 TECU, comparable to the EIA crest. In the second row, a strip of decreased hmF2, that is, ∼300 km, at −30 GLAT was between the southern EIA crest and the southern SED.

During the first southward IMF period, the convection pattern indicated by the ion velocity vectors expanded equatorward to lower latitudes, and their magnitudes increased significantly (Figures 2d–2f). Meanwhile, in the bottom row (Figures 2g and 2h), the enhanced energy input in the auroral region drove equatorward thermospheric wind, and the enhanced $\Sigma O/N_2$ region became narrower and moved equatorward compared to the quiet time in Figure 2g. Note that this enhanced $\Sigma O/N_2$ region overlapped the equatorward portion of the southern SED base as shown in Figures 2h and 2i.

After the IMF B_z turned northward at ∼22 UT, the TEC of the EIA crests in both hemispheres decreased, and the SED plumes in both hemispheres started to disappear due to the poleward retreat of the convection patterns and flow direction changed. Interestingly, the southern SED base expanded horizontally and kept moving equatorward, reaching the southern EIA crest, as shown in Figure 2c. In Figure 2f, in the northern hemisphere, there was a tilted strip of strong lifted ionosphere to ∼500 km across from noon to dusk at the middle latitude. Movie S1 shows the southwestward propagation of this perturbation from the auroral region. Hence, we suggest this is a manifestation of TAD/TID propagating from the enhanced energy input region and this contributed to the already elevated northern ionosphere even after the B_z turned northward. The distribution of the $\Sigma O/N_2$ ratio maintained hemispheric asymmetric, and the southern enhanced $\Sigma O/N_2$ region moved further equatorward, reaching −20 GLAT. This enhancement still overlapped with the equatorward portion of the strong southern SED base, indicating the equatorward wind as the common driver of both.

Besides the thermospheric composition indicated by $\Sigma O/N_2$ ratio, vertical plasma motion can also change the ionospheric density through altitude dependent chemical reaction rates. The three major components of vertical plasma drift are the vertical component of E × B drift, meridional neutral wind, and ambipolar diffusion, which all depend on the magnetic inclination and declination angles (Schunk & Nagy, 2000). To further understand the formation of the SED base and the contributions from each factor, we decompose the overall modeled ion upward flow into these three components and quantitatively evaluate their contributions.

Figure 3 shows the vertical plasma upward flow components at 360 km at the same time instances of Figure 2. This altitude is chosen because it is between the maximum NmF2 before and during the storm and the altitude profiles of the upward flow components show little variations within ∼300–500 km. Three rows from top to bottom are induced ion vertical drifts by neutral wind, E × B drift (including PPEF and DDEF), and ambipolar diffusion. The TEC contours are superposed on top of these panels.

Following the first B_z southward turning, Fejer et al. (2024) showed an increase in height-averaged Jicamarca vertical plasma drift in the early afternoon sector to ∼50 m/s due to the sudden PPEF. This was followed by another ∼30 min increment reaching ∼80 m/s at 19:30 UT on April 23 after a solar wind dynamic pressure increase. Our model results successfully captured the dayside PPEF induced vertical drift and showed similar enhancement magnitude to ∼50 m/s. However, the model did not capture the short-lived secondary increase due to solar wind dynamic pressure increase. Please see the time series of these dynamic variations in supporting Movie S1. The PPEF increase-induced vertical drift on the dayside after the southward turning can also be seen in

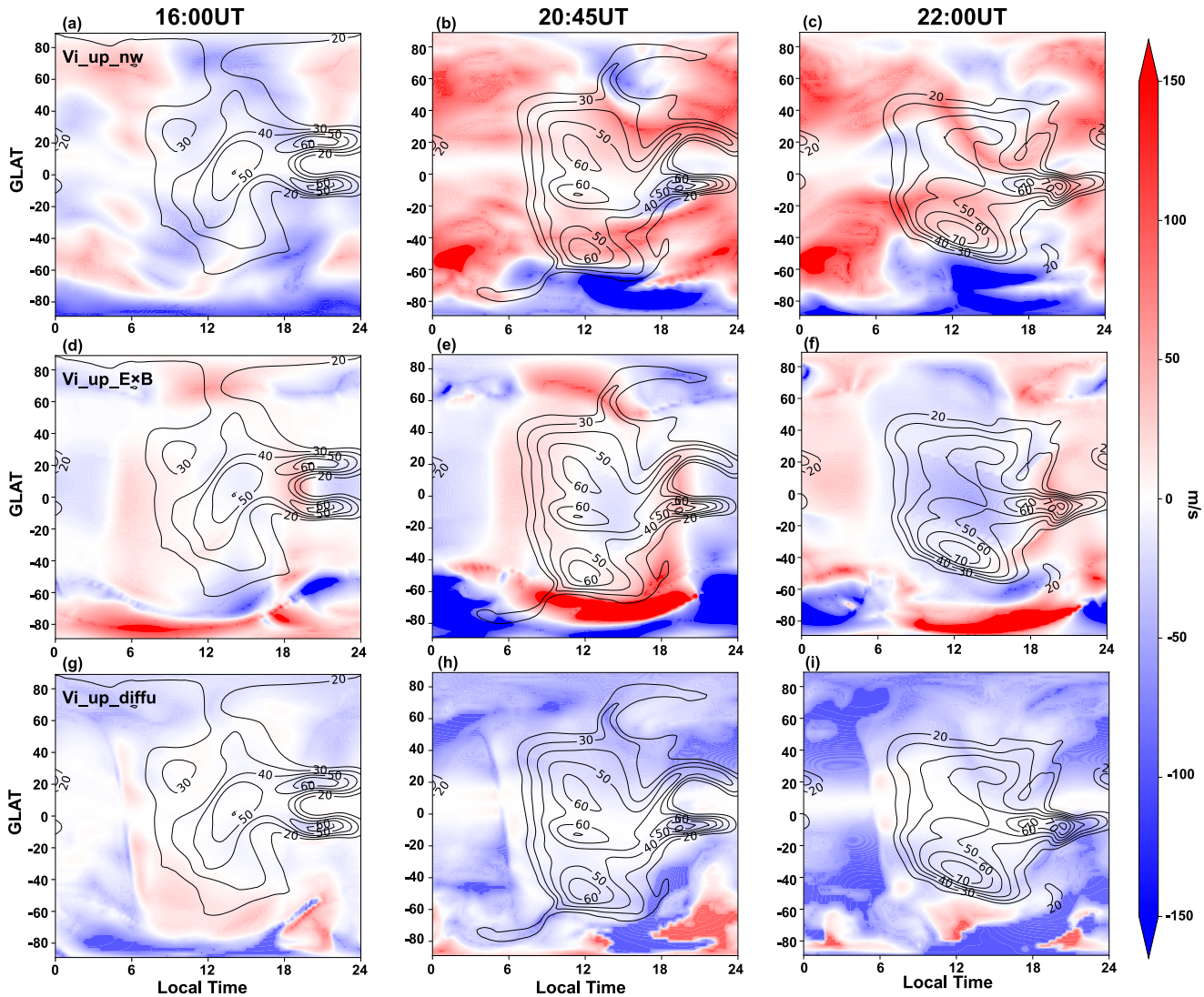


Figure 3. Contributions of plasma upflow from three different components of (a–c) neutral wind, (d–f) E × B drift, and (g–i) ambipolar diffusion with TEC contour lines. Calculations are shown at 360 km.

Figure 4c. The penetration electric field and the associated plasma drift are important for the widening of EIA during storms. Later at 20:45 UT, strong upward drifts due to neutral winds near the afternoon midlatitude region overlapped with both SED bases, suggesting their critical role in the formation of the SED base. Specifically, at the region around 17 LT seen in Figure 3e, the upward drift due to neutral wind exceeded over 120 m/s between −40° and −60° latitudes, contributing to the 500 km hmF2 shown in Figure 2. However, the upward drifts due to the E × B drift were confined in the poleward portion of the SED base and the plume region in Figure 3e.

At 22 UT under B_z northward conditions, the convection E field retreated poleward, and the corresponding drift became downward at low-midlatitude regions. During this time, the upward lift due to neutral wind maintained at ∼100 m/s while its peak moved to lower latitudes due to the southward propagating wind. Furthermore, the boundary of the positive vertical drift due to wind aligned well with the poleward boundary of the southern SED base from 8 to 16 LT. In the northern hemisphere, the strip of the lifted ionosphere discussed in Figure 2f matched the location of ∼120 m/s upward neutral wind drift. The above descriptions directly confirm that the equatorward neutral wind dominates the vertical transport of plasma to higher altitudes in the low- to midlatitude regions. During the B_z northward period (∼21-01 UT), model results show that the equatorial vertical plasma drift due to E × B is downward across 12–17 LT, which is consistent with the Jicamarca vertical drift shown in Fejer et al. (2024).

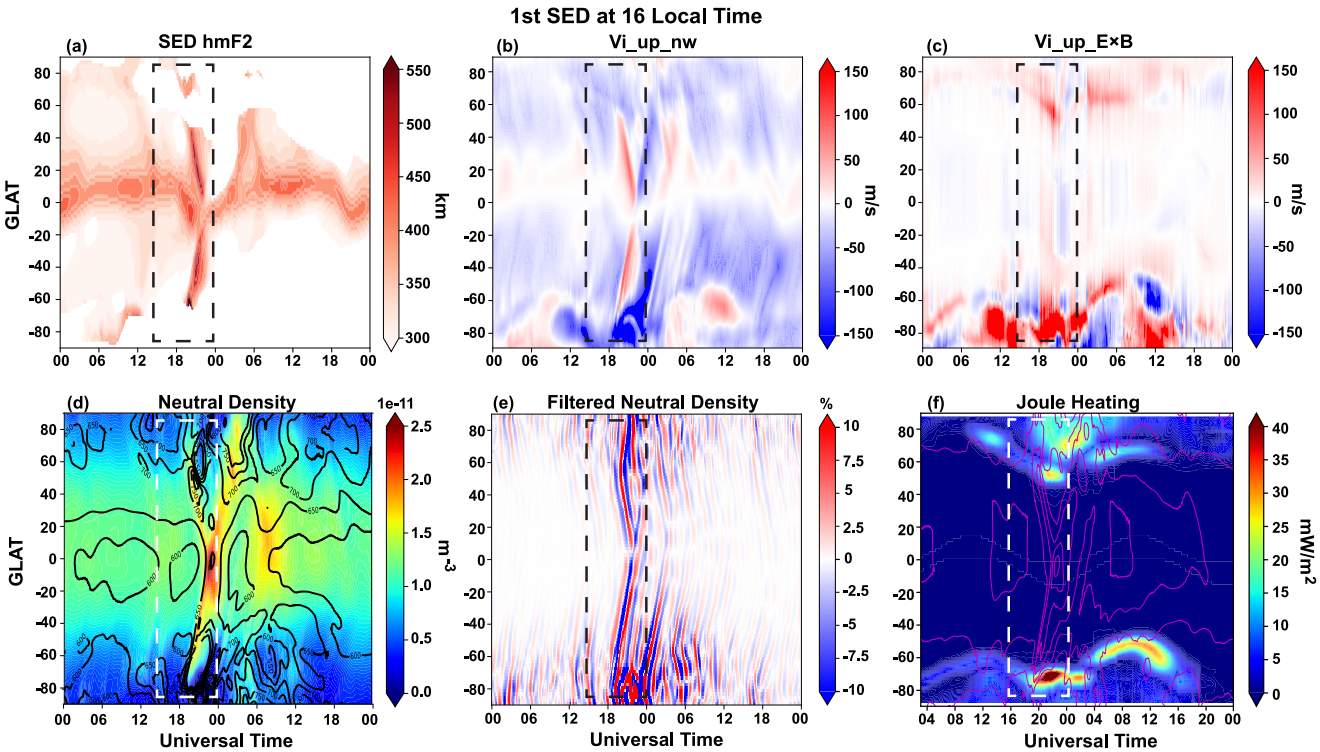


Figure 4. Keograms at 16 LT of (a) hmF2, (b) upward neutral wind drift and (c) upward drift by electric field, (d) neutral density at 360 km. Neutral temperature at 155 km is plotted as line contours. (e) Detrended neutral density. (f) Running average of previous 3-hr Joule heating from the IE output with line contours of neutral density at 360 km. Dashed squares highlight the SED period.

To further quantify the cumulative effect of different contributing factors to the upward drift, keograms of key parameters are shown in Figure 4. The first row of Figure 4 shows the keograms of the SED hmF2, upward ion drift due to neutral wind, and E × B drift at 16 LT, where the southern SED base peaks. Before the first B_z southward turning at ~18 UT on April 23rd, the hmF2 keogram showed a regular one-peak EIA with hmF2 at ~400 km. During the first B_z southward turning and the followed northward turning, that is, 18-01 UT, the SED hmF2 in both hemispheres increased, and both peaks moved equatorward. In Figure 4b, the upward ion drift induced by the neutral wind shows the same equatorward propagation feature.

The equatorward wind propagation feature originated from the auroral regions at ~18 UT and reached the magnetic equator at ~22 UT, lifting the plasma to higher altitudes. In contrast, the effect of the electric field was stronger (>100 m/s) at higher latitudes. At midlatitude, the vertical drift driven by the electric field was upward at ~70 m/s during the first southward B_z period and immediately turned downward as B_z became northward. Hemispheric asymmetry of the ion vertical drift due to the electric field can also be seen in Figure 4c with a stronger vertical drift speed in the southern hemisphere.

TIDs/TADs are wave-like perturbations and manifestations of the atmospheric gravity waves (AGW) (Hines, 1960; Hunsucker, 1982). Intense Joule heating energy input during storms causes the thermosphere to expand and triggers large-scale TADs propagating equatorward (Balthazor & Moffett, 1999; Lu et al., 2001; Prölss, 1993b). Via ion-neutral friction, TADs lead to ionospheric fluctuations, which are referred to as large-scale TIDs (Hocke & Schlegel, 1996; Richmond & Roble, 1979). Figure 4d shows the neutral density keogram at 360 km with neutral temperature at 155 km as line contours. The E-region neutral temperature increased due to enhanced auroral energy deposition collocated with the F-region neutral density increase and is plotted to show the initiation of the TADs. The neutral density at 360 km was further filtered using a second-order butterworth band-pass filter with cutoff periods of 30 and 120 min, which are typical for large-scale TAD/TIDs. Figure 4e shows this filtered density as a percentage difference between the original and filtered data. Averaged storm-time neutral density perturbation reached 12%, and these perturbations propagated equatorward in the form of TAD. The southern TAD successfully passed the equator and penetrated the northern hemisphere after the B_z

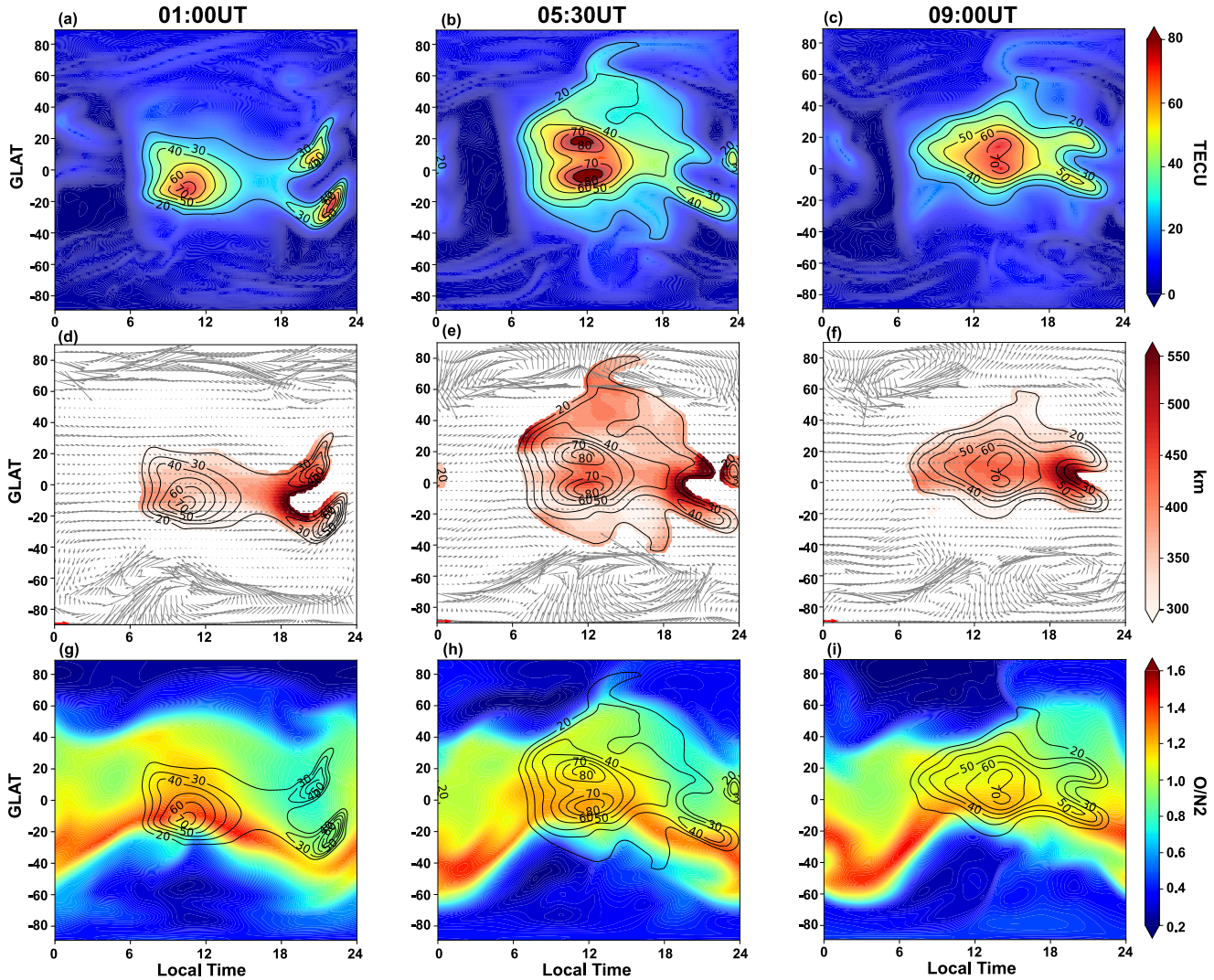


Figure 5. Formation and evolution of the second asymmetric SED base during the second ICME magnetic cloud southward IMF period. Same format as Figure 2.

northward turning; however, the northern TAD did not go through. The dominant periods for the TAD at ±50° were 1.54 hr. The same filter is applied to the GITM ion density at 360 km and reveals the ionospheric counterpart, that is, TID (not shown) with similar amplitude.

The hemispheric asymmetry of TADs/TIDs can be traced back to the input energy asymmetry. Since the time delay between Joule heating and neutral density perturbation is expected to be ~2–3 hr (Hong et al., 2023; Wang et al., 2020), we calculate the previous-3 hr running average of Joule heating at 16 LT and present it in Figure 4f together with contours of the neutral density from Figure 4d. It is clear that the southern Joule heating was stronger than the northern counterpart and the corresponding region excited the TADs that penetrated the northern hemisphere.

4.2. SED During the Second Southward IMF Period

The second southward B_z period from 01:40 UT to 11 UT on April 24th was due to the ICME magnetic cloud, which lasted longer and had a more negative B_z value than that of the ICME sheath. Figure 5 shows the evolution of the TEC, hmF2, and $\Sigma O/N_2$ in the same format as Figure 2. The disappearance of the first southern SED base at 22 UT on April 23rd lasted until early April 24th as the ionosphere entered a negative phase due to the O/N_2 ratio reduction in the midlatitude regions in both hemispheres. The lifted EIA remnants at dusk also decreased in terms of TECU, hmF2, and spatial coverage. Just before the second southward turning in Figure 5a, the dayside

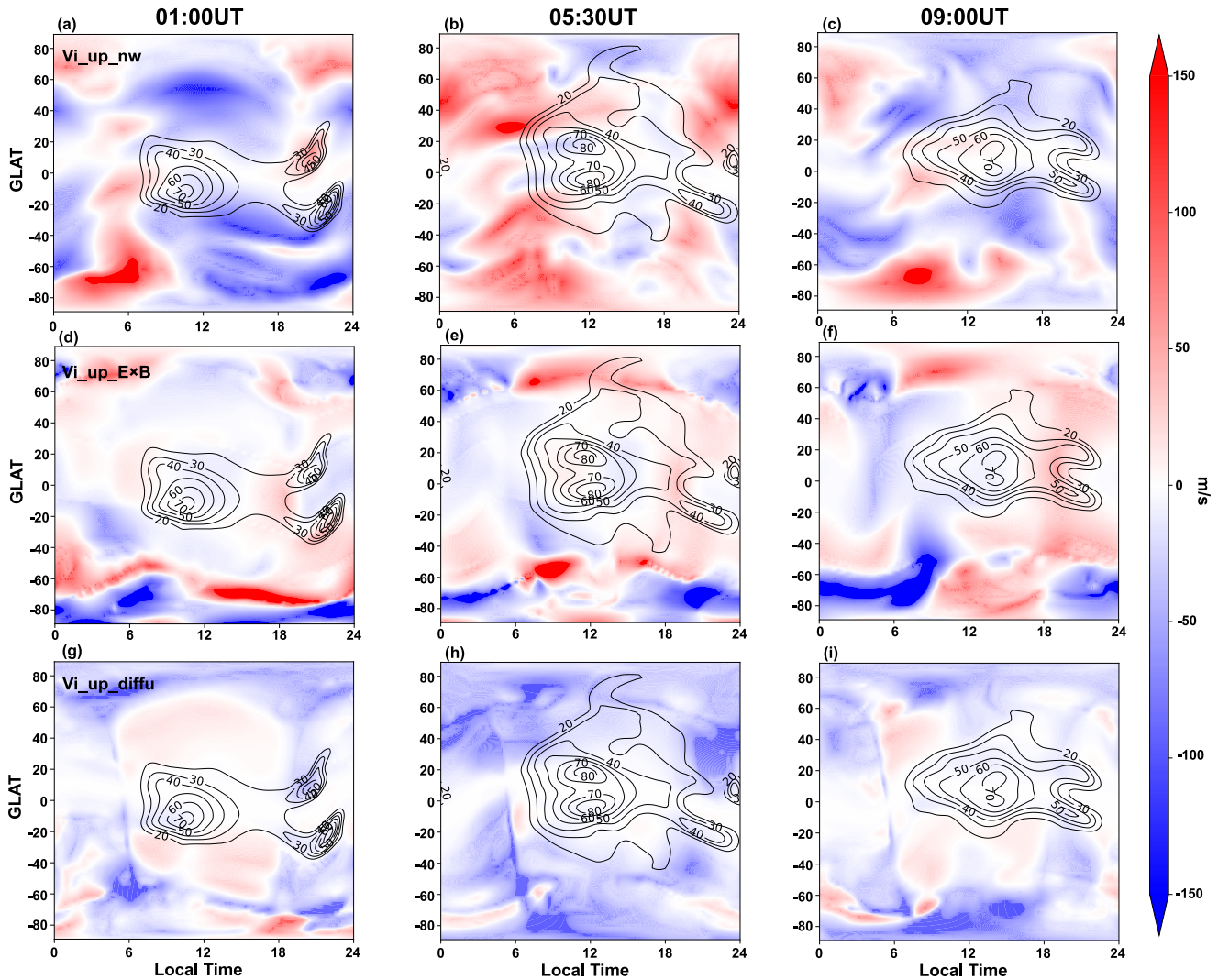


Figure 6. Evolution of plasma upflow for the second SED base at 360 km due to different components. The same format as Figure 3.

ionosphere at noon showed one peaked EIA region with hmF2 of ∼350 km. The $\Sigma O/N_2$ ratio decreased overall and its peak near the southern low latitudes dropped from over 1.6 in the previous day to ∼1.4.

At 5:30 UT, ∼4 hr after the second southward turning, the bifurcated EIA crests centered at 20° and −5° geographic latitudes. In the northern midlatitude region, an SED base with a plume formed above ∼40° latitude 12–16 LT. However, this second SED base was weaker than that during the first period with 30 TECU and lower hmF2 at ∼400 km. The weak northern plume penetrated into the polar region. In contrast, the southern hemisphere barely developed an SED base or plume. The dayside $\Sigma O/N_2$ further decreased to ∼1.2 at noon, and the boundary of the $\Sigma O/N_2$ enhancement aligned well with the northern SED and plume contours.

The northern SED base and plume started to decay at ∼9 UT, as shown in Figure 5c. The strong convection velocity vectors retreated to higher latitudes and deceased due to weakened southward IMF.

Figure 6 shows the decomposed ion upward drift at the same times as Figure 5 and in the same format as Figure 4. Before the second southward B_z turning, the neutral wind-driven ion vertical drift was ∼70 m/s downward with a rough north-south symmetry in the midlatitude regions, while the E × B drift component was negligible in the low-midlatitude regions. Thus, the overall downward drifts suppressed the lifting of plasma. At the peak of the storm, the vertical drift due to neutral wind was less hemispherically asymmetric compared to Figure 3b. The northern SED base was largely driven by the neutral wind-driven upward ion drift at ∼50 m/s, and the lifting due

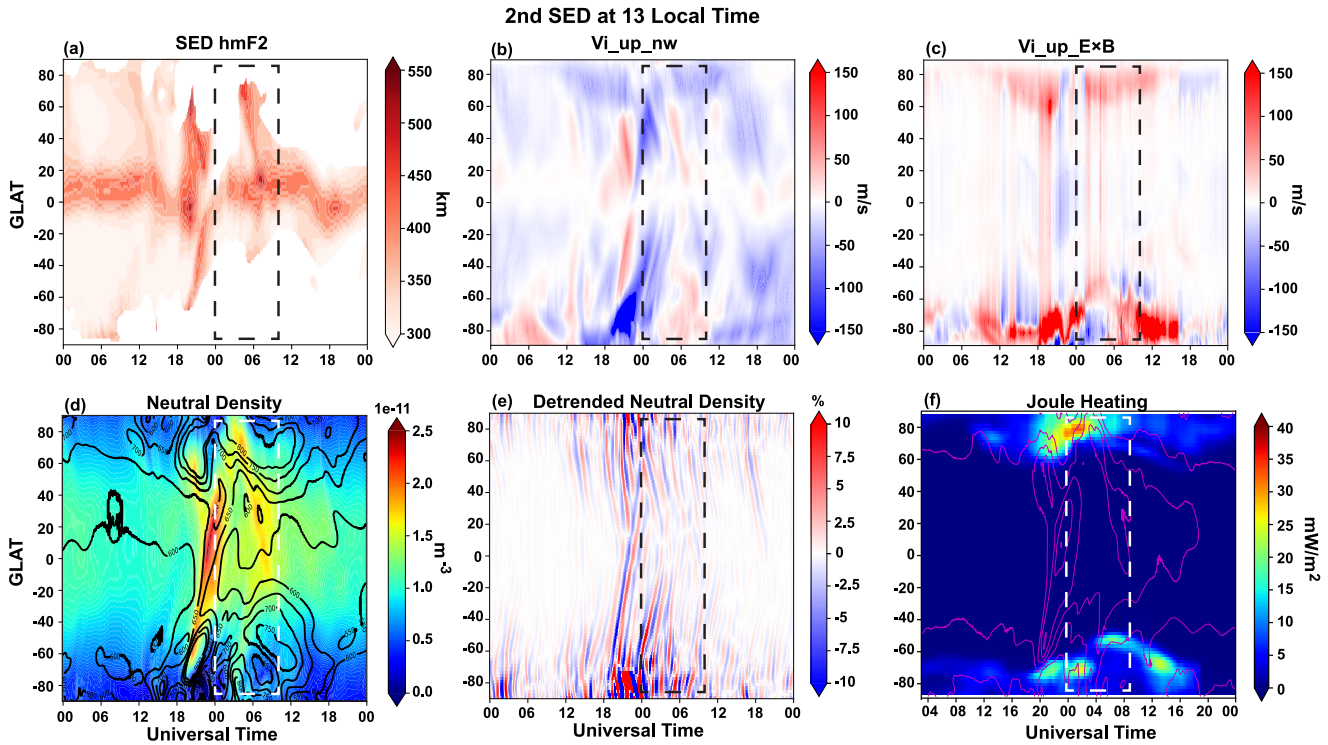


Figure 7. The same format as Figure 4 but at 13 LT for the second SED period.

to the E × B drift was confined to auroral latitudes. During the later recovery phase at 9 UT, the neutral wind component became downward in both hemispheres.

Figure 7 keeps the same format as Figure 5 but at 13 LT focusing on the second SED local time. As shown in Figure 7a, the lifted SED formation started in this LT sector around 03 UT after the second strong southward turning at 01:30 UT. The northern SED hmF2 reached ∼400 km, while the southern bulge only reached ∼320 km. The southward-propagating wind surge was well aligned with the increased hmF2 of the northern SED (Figure 7b). However, the upward ion drift induced by the neutral wind was much weaker compared to that at 16 LT during the first dip. In Figure 7c, the base of the northern SED was located at the equatorward edge of strong convection-driven ion drift, and there were short-lived penetration electric fields to low latitudes. Similar to the first period, the neutral wind contributed 25 m/s to the overall lifting speed, and the convection electric field played a minor role. The ion vertical drift due to the convection electric field remained hemispherically asymmetric near the subauroral and auroral zones.

During the second southward B_z turning, the neutral density perturbation shown in Figure 7d started at about the same time in both hemispheres but with larger perturbations in the northern hemisphere. The neutral density perturbation signature propagated southward toward the equator, arriving there at ∼08 UT. Despite the stronger IMF B_z during the second period, the neutral wind-induced upward drift was weaker than the first period. Since the ionosphere entered the negative phase, the overall interaction between neutrals and ions became less efficient due to the lower plasma density. Also, since the keogram focusing on the second episode of SED at 13 LT, which is closer to noon compared to Figure 4 at 16 LT, the high latitude equatorward wind at the dayside needed to overcome the stronger solar EUV produced poleward wind to produce the final equatorward wind at this local time.

Using the same filtering, Figure 7e shows the detrended neutral density. In this case, the average perturbation percentage is only 5%. We found that the dominant TAD period was also longer, that is, at 2 hr for both hemispheres. The corresponding TID at 360 km also had a smaller perturbed amplitude within 5% at middle latitudes. At noon around 13 LT, the northern hemisphere averaged Joule heating was much stronger than that in the south hemisphere, which is consistent with the larger neutral density perturbations in the northern hemisphere

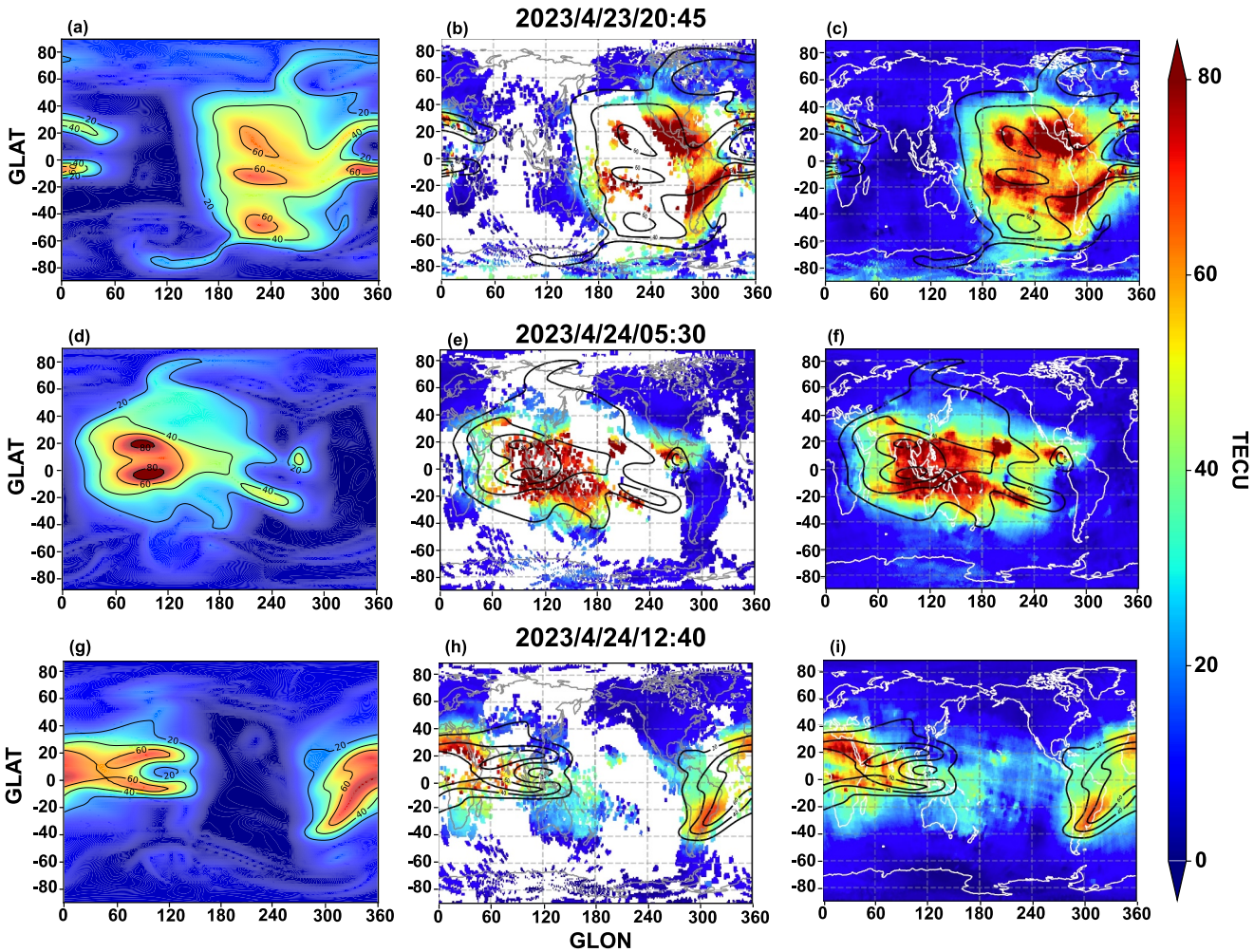


Figure 8. Global TEC maps comparison between GITM (a, d, g), Madrigal and GOLD (b, e, h) and VISTA (c, f, i) at three instances.

shown in Figure 7d. During 04–08 UT, there was another episode of moderate Joule heating at ∼−50° latitude, but it did not excite any clear regional equatorward propagating TAD in Figure 7d.

4.3. Model-Observation Comparison

To validate the accuracy of GITM results driven by the IE outputs from the Geospace Model, model-data comparison of TEC maps at three instances is provided in Figure 8. The first column shows the GITM TEC maps. The middle column shows the global-scale vertical TEC data from the CEDAR Madrigal database (Rideout & Coster, 2006; Vierinen et al., 2016). Despite increasing numbers of ground-based GNSS receivers, the 2D global TEC maps still contain large data gaps, especially over the oceans and the south hemisphere. To increase the data coverage, GNSS data has been supplemented with TEC derived from Global-scale Observation of the Limb and Disk (GOLD) satellite ultraviolet spectrometer observations (Cai et al., 2020; Eastes et al., 2020). The GOLD mission provides the 135.6 nm emission due to radiative recombination and thus can be used to infer the nightside F-region peak density NmF2 and TEC. More details about the methodology of inferring TEC based on the GOLD emission can be found in Qin et al. (2023). In our study, we further calibrated the GOLD TEC with Madrigal TEC at their overlapping points and then applied the calibration to other non-overlapping GOLD points. In this particular event, the impact of GOLD TEC is limited because the GOLD field-of-view is outside the targeted SED region. VISTA (Video Imputation with SoftImpute, Temporal smoothing and Auxiliary data) developed by Sun et al. (2021) is a TEC matrix completion tool which fills in the gaps and preserves the observed meso-scale TEC features. The combined Madrigal and GOLD TEC are used as inputs for the VISTA algorithm,

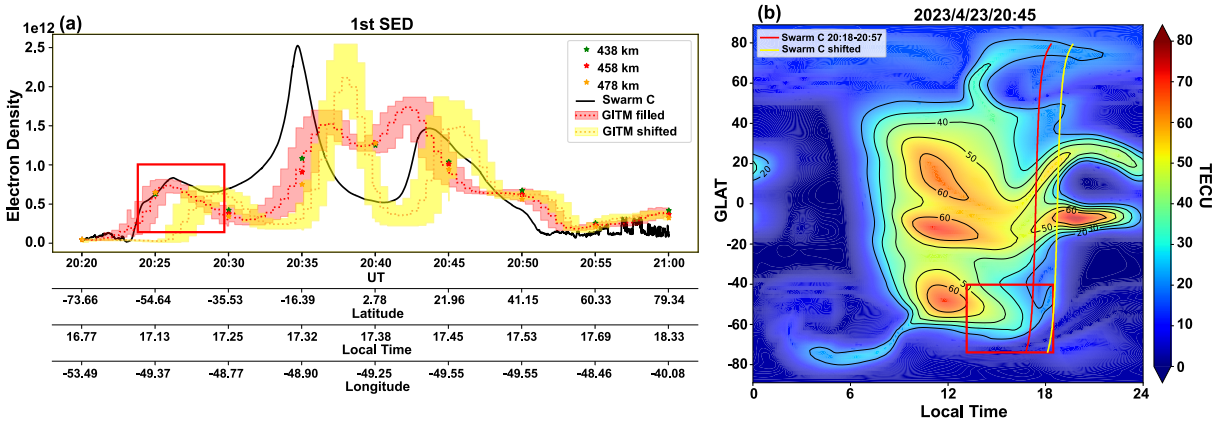


Figure 9. (a) Swarm C measured electron density at 462 km (black line), GITM density from the simulation grids centered at 438, 458, and 478 km (green, red, and yellow stars), approximated GITM density along the Swarm C trajectory with uncertainties (red dotted line and shade) assuming stationary within 5 min, and GITM density along a shifted trajectory by 20° glon (yellow dotted line and shade) during the first SED period. (b) Global maps of TEC overlapped with SWARM trajectory and the shifted trajectory.

and the results are shown in the third column. Contours of modeled TEC are overlapped on the columns of GNSS observation and VISTA TEC. Movie S2 in the Supporting Information shows the full 2-day event TEC comparison in the same format as Figure 8. Note that the GITM TEC only contains electrons from the GITM lower boundary (~100 km) to the upper boundary (~700 km), while the TEC measurements include electrons between the receivers and the GNSS satellites (~20,000 km). Therefore, qualitative comparisons between these two are conducted to confirm the general trend and large- and meso-scale structures.

The three TEC cadences are selected during the first southward turning (top row), the second southward turning (middle row), and the storm recovery phase (last row). In the top row, at 20:45 UT on April 23rd, the large-scale widened EIA revealed by the raw Madrigal TEC and the VISTA map was successfully reproduced by GITM near the equatorial regions. In the midlatitude regions, the asymmetry between the northern and southern SEDs is confirmed by the TEC data. Due to the sparse GNSS data coverage over the southern Pacific Ocean, the peak of the southern SED was not clear in the VISTA map. However, GITM captured the northern SED plume over the Alaska and Arctic, which were observed by the GNSS TEC data. This short-lived north plume was also confirmed and studied by Aa et al. (2024).

During the second southward turning in Figures 8d–8f, both GITM and observation showed a more latitudinally narrow EIA within ±20°, and the southern EIA was stronger than its northern counterpart. In the late recovery phase (Figures 8g–8i), a striking single-peak EIA before 12 LT was revealed by the GNSS TEC data over the South American continent and successfully reproduced in GITM.

Due to the limitation of the raw GNSS coverage over the critical SED region, we expand the data-model comparison by including the SWARM in situ measurement in Figure 9. Swarm C measured the electron densities at ~462 km near 17 LT during the first SED period (Figure 9a). The GITM data are saved at a 5 min cadence and the colored stars in Figure 9a are the GITM simulated density at those times from simulation grids around the Swarm C altitude. We assume that the ionosphere density doesn't change significantly within 5 min and thus extract the modeled density to fill in the gaps along the satellite trajectory. The averaged density from the nearest simulation grids surrounding the satellite location in height, latitude and longitude is plotted as a red dotted line, and the range of the density values from the surrounding grids is shaded in red. Figure 9b shows the corresponding global GITM TEC map overlapped with the Swarm C trajectory and the trajectory after shifting 20° glon eastward. At 20:27 UT, Swarm C detected the isolated southern SED peak at −50° glat and at 17 LT, and the modeled density matches well with the observation at ~7e11/m^3 as highlighted with a red square box.

In general, validating 2D simulation results with a 1D satellite pass presents a significant challenge due to the complexity of the spatial and temporal variations of the phenomena. For example, Swarm C showed two distinct EIA peaks at 17 LT with higher density in the southern EIA, while the modeled density at this LT (Figure 9a red curve) did not capture this hemispheric asymmetry. However, the modeled 2D TEC indeed shows higher southern EIA crest values at slightly later LT. After shifting the Swarm C trajectory to ~1.3 hr of LT later, the model

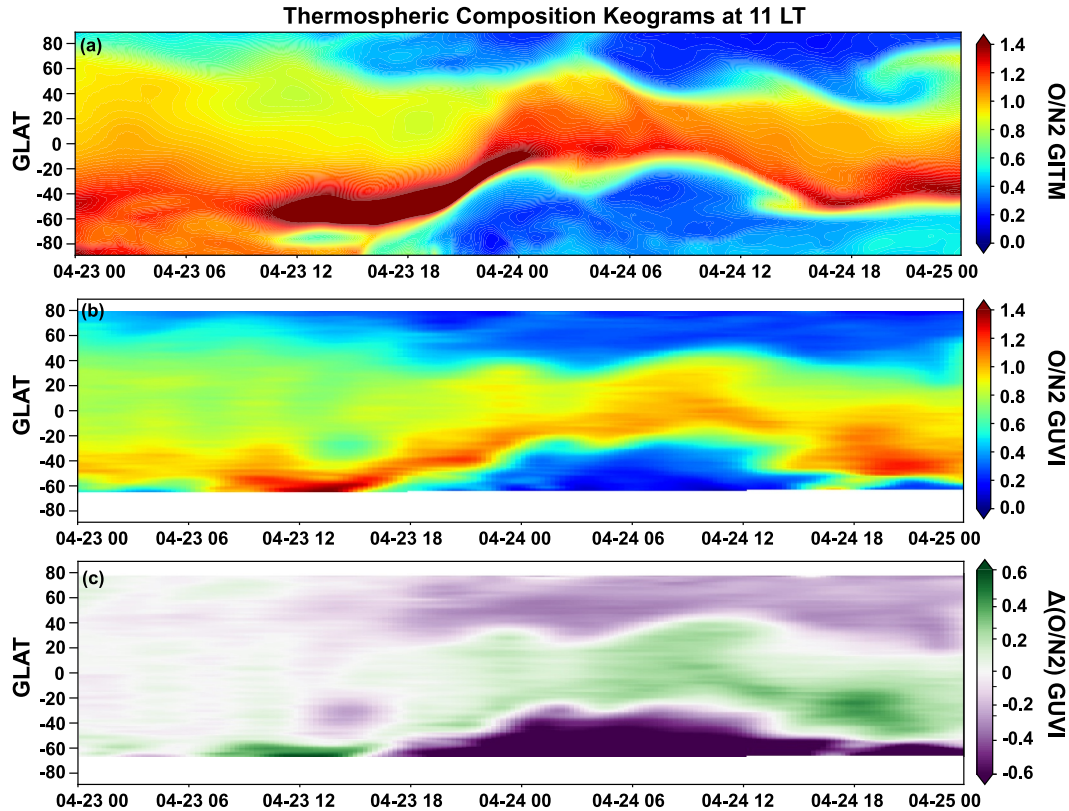


Figure 10. Thermospheric composition keograms at 11 LT of (a) $\Sigma O/N_2$ ratio from GITM; and (b) $\Sigma O/N_2$ ratio from GUVI. The previous 3-day of GUVI observations were averaged and subtracted to show the perturbation of the GUVI data on the storm day. (c) The change of O/N_2 ratio from GUVI observation.

revealed a stronger southern EIA (Figure 9a yellow curve). Keeping those challenges in mind, we emphasize that the single satellite pass here is mainly aimed to confirm the existence of the distinct southern SED peak.

Understanding the constraints of the TEC comparison, we further compare the observed and modeled thermospheric O/N_2 ratios. The observed $\Sigma O/N_2$ is obtained by the Thermosphere, Ionosphere, Mesosphere Energetics and Dynamics (TIMED) Global Ultraviolet Imager (GUVI). The GUVI column density ratio of $\Sigma O/N_2$ is derived from the OI 135.6 nm and the N_2 Lyman-Birge-Hopfield emissions (Strickland et al., 1995; Zhang et al., 2004) and has been widely used to infer the competition between the O^+ production and the dissociative recombination loss processes, which are directly related to the global TEC (Meier, 2021). Figure 10 shows the keograms of $\Sigma O/N_2$ from GITM and GUVI at 11 LT. Before the ICME arrival, the thermospheric $\Sigma O/N_2$ ratio showed higher values in the southern hemisphere than those in the northern hemisphere, consistent with large-scale seasonal hemispheric asymmetry (Forbes, 2007). After the ICME shock arrival at ∼18 UT on April 23rd, the enhanced $\Sigma O/N_2$ ratio moved equatorward in both hemispheres. Shown by both GUVI and GITM, the significant hemispheric asymmetry started early on April 24 as the depleted $\Sigma O/N_2$ region reached −20° latitudes in the south but was at >+40° in the north. Subtracted by the previous 3-day quite time average value, the storm time deviation of $\Sigma O/N_2$, that is, $\Delta(O/N_2)$, in Figure 10c, also revealed the stronger depletion in the south. Interestingly, Habarulema et al. (2024) showed the absence of HF echoes at Grahamstown (UTC + 2) in the southern hemisphere during the magnetic cloud period and attributed it to the strong storm negative phase, suggesting a tilted F-region. Therefore, in general, the simulated $\Sigma O/N_2$ agrees with observations well, demonstrating the high fidelity of the GITM simulation.

5. Discussion and Conclusions

In this study, we identified two periods of SED and plume during the double-dip April 23–24, 2023 storm and analyzed their formation and evolution considering the combined effects of thermospheric composition changes

and induced ion upward drifts. We further decomposed the ion upward drifts and quantified the contributions of the equatorward wind, convection electric field, and diffusion. The formation and propagation of TID/TAD within SED has also been studied.

The two episodes of SEDs were ultimately caused by the southward IMF within the ICME sheath and magnetic cloud of this ICME structure. During the first ICME sheath B_z southward period, SEDs formed in both hemispheres with the southern SED more prominent than the northern counterpart, while only the northern SED formed during the second B_z southward period, that is, the magnetic cloud period. Decomposing the induced upward ion drifts within SED into neutral wind, E × B drift, and ambipolar diffusion driven components, we found that the upward neutral wind-driven component is the determining factor for the midlatitude lifted SED bases, and the convection electric field is more important for the SED and plume at subauroral and auroral latitudes, which are consistent with other storm studies (Lu et al., 2012; Zou et al., 2013, 2014).

During the first southward IMF period, enhanced Joule heating in the high latitude region led to impulsive thermospheric wind propagating equatorward and westward in both hemispheres, which facilitated the upward ion drifts. The TAD/TID signatures were also identified within the wind surge and contributed to about 10% of the density perturbations. Even after the IMF northward turning within the ICME sheath, the strong wind initiated in the southern hemisphere continued to propagate northward across the equator, suppressing the uplifting in the northern hemisphere. The equatorward wind initiated in the northern hemisphere was weaker and did not propagate to the other hemisphere. Furthermore, our study supports one of Wang et al. (2021) findings that the magnitude of TID was larger in the hemisphere where the negative storm phase developed later, as the southern hemisphere entered a more significant negative phase in the second period.

Despite the fact that the B_z during the magnetic cloud was twice as negative as that during the first period, the SED during the second episode was much weaker than during the first, and the southern SED barely formed. The different responses of the SEDs during the two southward IMF periods and the reversal of their hemispheric asymmetries, that is, from a stronger southern SED during the first period to a stronger northern SED during the second period, can be attributed to the complex thermospheric composition change throughout these 2 days, including pre-storm modulation, storm reinforcement, and the hemispheric asymmetry of magnetic pole offset as well as its associated UT dependence.

1. Pre-storm modulation: The storm occurred in late April and the $\Sigma O/N_2$ was stronger in the winter (southern) hemisphere due to seasonal effect. In addition, before the ICME arrival, the IMF was already slightly southward for hours, leading to some weakly enhanced $\Sigma O/N_2$ near the southern auroral zone.
2. Storm reinforcement: During storm time, further enhanced $\Sigma O/N_2$ occurred in the southern subauroral zone due to the meso-scale neutral circulation induced by the auroral zone energy input (Forbes, 2007). This enhanced $\Sigma O/N_2$ ratio provided ample neutral source to be photoionized, and thus, the plasma production dominates the chemical loss. Therefore, a stronger southern SED could form near the peak $\Sigma O/N_2$ ratio region. This enhancement was isolated from the southern EIA crest, forming a distinct SED base peak.
3. Magnetic pole offset and UT effects: During the magnetic cloud period, strong convection and auroral oval with enhanced Joule heating expanded further to midlatitude near local noon in the southern hemisphere than their northern counterparts due to the asymmetric offset between magnetic and geographic poles in the two hemispheres. This expansion pushed the enhanced O/N_2 to lower latitudes in the southern hemisphere and created large convection and equatorward wind to induce ion upward drift. Yet, the southern SED barely formed. Instead, the northern SED dominated during this period. This is because the region with the enhanced $\Sigma O/N_2$ in the southern hemisphere moved to near the equator, far from where the high-latitude convection and wind could reach. Meanwhile, the reduced $\Sigma O/N_2$ in southern midlatitude region signaled severe thermosphere composition changes and prohibited the southern SED growth due to reduced production but increased loss process. However, in the northern hemisphere, the $\Sigma O/N_2$ in the midlatitude was relatively larger so an SED can still develop.

The effect of IT preconditioning due to thermosphere composition was previously studied for the 2003 and 2004 superstorms driven by multiple ICMEs (Verkhoglyadova et al., 2017). The current study reveals that even within the same ICME, a significant energy input during the ICME sheath can alter the thermosphere composition rapidly and significantly, which leads to a much weaker second positive ionospheric storm during the subsequent magnetic cloud period.

To summarize, the two episodes of opposite hemispheric-dominated SED during the ICME sheath and magnetic cloud were mostly driven by the neutral wind-induced upward ion drift in the midlatitudes and convection induced upward drift in the sub-auroral and auroral zones. The stronger southern SED in the first period was primarily due to excessive plasma production indicated by the enhanced $\Sigma O/N_2$ ratio because of a combination of pre-storm modulation and storm reinforcement. During the magnetic cloud period, the offset of magnetic and geographic poles in the south hemisphere and the associated UT effect led to stronger convection and Joule heating near the southern noon and thus larger induced ion drift. However, the collocated low $\Sigma O/N_2$ ratio limited the development of the southern SED, and on the contrary, a weak northern SED successfully developed. Large-scale TAD/TIDs formed but played a minor role in both episodes.

Data Availability Statement

The raw GPS TEC data used are available at the Madrigal database (CEDAR Madrigal Database, 2022). The solar wind speed and IMF data are obtained from the NASA GSFC Space Physics Data Facility's OmniWeb (https://omniweb.gsfc.nasa.gov/html/omni_min_data.html) (Papitasgvili & King, 2025). The geomagnetic index SYM-H is downloaded from the World Data Center in Kyoto (https://wdc.kugi.kyoto-u.ac.jp, 2025). The GUVI data are available at https://guvitimed.jhuapl.edu/ (Global UltraViolet Imager, 2025). The GITM model is open source at https://github.com/GITMCode/GITM (Ridley et al., 2006). Space Weather Modeling Framework is open source at https://github.com/SWMFsoftware (Gombosi et al., 2021).

Acknowledgments
This work is supported by NASA LWS 80NSSC20K0190, NASA HSR 80NSSC20K1313, and NASA 80NSSC23K0407.

References

Aa, E., Zhang, S.-R., Zou, S., Wang, W., Wang, Z., Cai, X., et al. (2024). Significant midlatitude bubble-like ionospheric super depletion structure (BLISS) and dynamic variation of storm-enhanced density plume during the 23 April 2023 geomagnetic storm. *Space Weather*, *22*(3), e2023SW003704. https://doi.org/10.1029/2023SW003704

Anderson, D. N. (1976). Modeling the midlatitude F-region ionospheric storm using east-west drift and a meridional wind. *Planetary and Space Science*, *24*(1), 69–77. https://doi.org/10.1016/0032-0633(76)90063-5

Aol, S., Habyarimana, V., Mungufeni, P., Buchert, S. C., & Habarulema, J. B. (2024). Ground and space-based response of the ionosphere during the geomagnetic storm of 02–06 November 2021 over the low-latitudes across different longitudes. *Advances in Space Research*, *73*(6), 3014–3032. https://doi.org/10.1016/j.asr.2023.12.032

Astafyeva, E., Bagiya, M. S., Förster, M., & Nishitani, N. (2020). Unprecedented hemispheric asymmetries during a surprise ionospheric storm: A game of drivers. *Journal of Geophysical Research: Space Physics*, *125*(3), e2019JA027261. https://doi.org/10.1029/2019JA027261

Balthazor, R. L., & Moffett, R. J. (1999). Morphology of large-scale traveling atmospheric disturbances in the polar thermosphere. *Journal of Geophysical Research*, *104*(A1), 15–24. https://doi.org/10.1029/1998JA900039

Blanc, M., & Richmond, A. D. (1980). The ionospheric disturbance dynamo. *Journal of Geophysical Research*, *85*(A4), 1669–1686. https://doi.org/10.1029/JA085iA04p01669

Buonsanto, M. J. (1995a). Millstone Hill incoherent scatter F region observations during the disturbances of June 1991. *Journal of Geophysical Research*, *100*(A4), 5743–5755. https://doi.org/10.1029/94JA03316

Buonsanto, M. J. (1995b). A case study of the ionospheric storm dusk effect. *Journal of Geophysical Research*, *100*(A12), 23857–23869. https://doi.org/10.1029/95JA02697

Buonsanto, M. J. (1999). Ionospheric storms—A review. *Space Science Reviews*, *88*(3–4), 563–601. https://doi.org/10.1023/A:1005107532631

Cai, X., Burns, A. G., Wang, W., Qian, L., Solomon, S. C., Eastes, R. W., et al. (2020). The two-dimensional evolution of thermospheric ∑O/N2 response to weak geomagnetic activity during solar-minimum observed by GOLD. *Geophysical Research Letters*, *47*(18), e88838. https://doi.org/10.1029/2020GL088838

CEDAR Madrigal Database. (2022). (Version Madrigal 3.2.6 release) [Dataset]. *MIT Haystack Observatory*. http://cedar.openmadrigal.org/

Chamberlin, P. C., Eparvier, F. G., Knoer, V., Leise, H., Pankratz, A., Snow, M., et al. (2020). The flare irradiance spectral model–version 2 (FISM2). *Space Weather*, *18*(12), e2020SW002588. https://doi.org/10.1029/2020SW002588

Conte, J. F., Chau, J. L., Stober, G., Pedatella, N., Maute, A., Hoffmann, P., et al. (2017). Climatology of semidiurnallunar and solar tides at middle and high latitudes: Interhemispheric comparison. *Journal of Geophysical Research: Space Physics*, *122*(7), 7750–7760. https://doi.org/10.1002/2017JA024396

Coster, A. J., & Foster, J. (2007). Space-weather impacts of the sub-auroral polarization stream. *URSI Radio Science Bulletin*, *2007*(321), 28–36.

Crowley, G., Hackert, C. L., Meier, R. R., Strickland, D. J., Paxton, L. J., Pi, X., et al. (2006). Global thermosphere-ionosphere response to onset of 20 November 2003 magnetic storm. *Journal of Geophysical Research*, *111*(A10), A10S18. https://doi.org/10.1029/2005JA011518

De Zeeuw, D. L., Sazykin, S., Wolf, R. A., Gombosi, T. I., Ridley, A. J., & Tóth, G. (2004). Coupling of a global MHD code and an inner magnetospheric model: Initial results. *Journal of Geophysical Research*, *109*(A12), A12219. https://doi.org/10.1029/2003JA010366

Dhadly, M., Emmert, J., Drob, D., Conde, M., Doornbos, E., Shepherd, G., et al. (2017). Seasonal dependence of northern high-latitude upper thermospheric winds: A quiet time climatological study based on ground-based and space-based measurements. *Journal of Geophysical Research: Space Physics*, *122*(2), 2619–2644. https://doi.org/10.1002/2016JA023688

Doherty, P., Coster, A. J., & Murtagh, W. (2004). Space weather effects of October–November 2003. *GPS Solutions*, *8*(4), 267–271. https://doi.org/10.1007/s10291-004-0109-3

Eastes, R. W., McClintock, W. E., Burns, A. G., Anderson, D. N., Andersson, L., Aryal, S., et al. (2020). Initial observations by the GOLD mission. *Journal of Geophysical Research: Space Physics*, *125*(7), e27823. https://doi.org/10.1029/2020JA027823

Erickson, P., Goncharenko, L., Nicolls, M., Ruohoniemi, M., & Kelley, M. (2010). Dynamics of North American sector ionospheric and thermospheric response during the November 2004 superstorm. *Journal of Atmospheric and Solar-Terrestrial Physics*, *72*(4), 292–301. https://doi.org/10.1016/j.jastp.2009.04.001

Eriksson, S., Bonnell, J. W., Blomberg, L. G., Ergun, R. E., Marklund, G. T., & Carlson, C. W. (2002). Lobe cell convection and field-aligned currents poleward of the region 1 current system. *Journal of Geophysical Research*, *107*(A8), SMP16–1–SMP16–15. https://doi.org/10.1029/2001ja005041

Fejer, B. G., Laranja, S. R., & Condor, P. (2024). Multi-process driven unusually large equatorial perturbation electric fields during the April 2023 geomagnetic storm. *Frontiers in Astronomy and Space Sciences*, *11*, 1351735. https://doi.org/10.3389/fspas.2024.1351735

Fejer, B. G., Spiro, R. W., Wolf, R. A., & Foster, J. C. (1990). Latitudinal variation of perturbation electric fields during magnetically disturbed periods: 1986 SUNDIAL observations and model result. *Annals of Geophysics*, *8*, 441–454.

Forbes, J. M. (2007). Dynamics of the thermosphere. *Journal of the Meteorological Society of Japan*, *85B*, 193–213. https://doi.org/10.2151/jmsj.85b.193

Förster, M., Rentz, S., Köhler, W., Liu, H., & Haaland, S. E. (2008). IMF dependence of high-latitude thermospheric wind pattern derived from CHAMP cross-track measurements. *Annales Geophysicae*, *26*(6), 1581–1595. https://doi.org/10.5194/angeo-26-1581-2008

Foster, J. C. (1993). Storm-time plasma transport at middle and high latitudes. *Journal of Geophysical Research*, *98*(A2), 1675–1689. https://doi.org/10.1029/92JA02032

Foster, J. C., Zou, S., Heelis, R. A., & Erickson, P. J. (2021). Ionospheric storm-enhanced density plumes. In C. Huang, G. Lu, Y. Zhang, & L. J. Paxton (Eds.), *Ionosphere dynamics and applications*. https://doi.org/10.1002/9781119815617.ch6

Fuller-Rowell, T. J., Codrescu, M. V., Moffett, R. J., & Quegan, S. (1994). Response of the thermosphere and ionosphere to geomagnetic storms. *Journal of Geophysical Research*, *99*(A3), 3893–3914. https://doi.org/10.1029/93JA02015

Fuller-Rowell, T. J., & Evans, D. S. (1987). Height-integrated Pedersen and Hall conductivity patterns inferred from the TIROS-NOAA satellite data. *Journal of Geophysical Research*, *92*(A7), 7606–7618. https://doi.org/10.1029/JA092iA07p07606

Ghag, K., Raghav, A., Bhaskar, A., Soni, S. L., Sathe, B., Shaikh, Z., et al. (2024). Quasi-planar ICME sheath: A cause of first two-step extreme geomagnetic storm of 25th solar cycle observed on 23 April 2023. *Advances in Space Research*, *73*(12), 6288–6297. https://doi.org/10.1016/j.asr.2024.03.011

Global UltraViolet Imager (2025). Retrieved from: https://guvitimed.jhuapl.edu/

Gombosi, T. I., Chen, Y., Glocer, A., Huang, Z., Jia, X., Liemohn, M. W., et al. (2021). What sustained multi-disciplinary research can achieve: The space weather modeling framework. *Journal of Space Weather and Space Climate*, *11*, 42. https://doi.org/10.1051/swsc/2021020

Grocott, A., & Milan, S. E. (2014). The influence of IMF clock angle timescales on the morphology of ionospheric convection. *Journal of Geophysical Research: Space Physics*, *119*(7), 5861–5876. https://doi.org/10.1002/2014JA020136

Habarulema, J. B., Zhang, Y., Matamba, T., Buresova, D., Lu, G., Katamzi-Joseph, Z., et al. (2024). Absence of high frequency echoes from ionosondes during the 23–25 April 2023 geomagnetic storm; what happened? *Journal of Geophysical Research: Space Physics*, *129*(3), e2023JA032277. https://doi.org/10.1029/2023JA032277

Hagan, M. E., & Forbes, J. M. (2003). Migrating and nonmigrating semidiurnal tides in the upper atmosphere excited by tropospheric latent heat release. *Journal of Geophysical Research*, *108*(A2), 1062. https://doi.org/10.1029/2002JA009466

Heelis, R. A. (2016). Longitude and hemispheric dependencies in storm-enhanced density. In T. Fuller-Rowell, E. Yizengaw, P. H. Doherty, & S. Basu (Eds.), *Ionospheric space weather: Longitude and hemispheric dependences and lower atmosphere forcing*. John Wiley & Sons, Inc. https://doi.org/10.1002/9781118929216.ch5

Heelis, R. A., Sojka, J. J., David, M., & Schunk, R. W. (2009). Storm time density enhancements in the middle-latitude dayside ionosphere. *Journal of Geophysical Research*, *114*(A3), A03315. https://doi.org/10.1029/2008JA013690

Hines, C. O. (1960). Internal atmospheric gravity waves at ionospheric heights. *Canadian Journal of Physics*, *38*(11), 1441–1481. https://doi.org/10.1139/p60-150

Hocke, K., & Schlegel, K. (1996). A review of atmospheric gravity waves and travelling ionospheric disturbances: 1982–1995. *Annals of Geophysics*, *14*(9), 917–940. https://doi.org/10.1007/s00585-996-0917-6

Hong, Y., Deng, Y., Zhu, Q., Maute, A., Hairston, M. R., Waters, C., et al. (2023). Interhemispheric asymmetries in high-latitude electrodynamic forcing and the thermosphere during the October 8–9, 2012, geomagnetic storm: An integrated data–Model investigation. *Frontiers in Astronomy and Space Sciences*, *10*, 1062265. https://doi.org/10.3389/fspas.2023.1062265

Hunsucker, R. D. (1982). Atmospheric gravity waves generated in the high-latitude ionosphere: A review. *Reviews of Geophysics and Space Physics*, *20*(2), 293–315. https://doi.org/10.1029/RG020i002p00293

Kalita, B. R., Bhuyan, P. K., Choudhary, M., Chakrabarty, D., Tiwari, R. C., Le. Huy, M., et al. (2024). The differential conjugate hemisphere ionospheric response during solstice storms and the winter side Maxima. *Advances in Space Research*, *73*(3), 1893–1907. https://doi.org/10.1016/j.asr.2023.11.025

Kalita, B. R., Bhuyan, P. K., Nath, S. J., Choudhury, M. C., Chakrabarty, D., Wang, K., et al. (2022). The investigation on daytime conjugate hemispheric asymmetry along 100°E longitude using observations and model simulations: New insights. *Advances in Space Research*, *69*(10), 3726–3740. https://doi.org/10.1016/j.asr.2022.02.058

Kelley, M. C., Vlasov, M. N., Foster, J. C., & Coster, A. J. (2004). A quantitative explanation for the phenomenon known as storm-enhanced density. *Geophysical Research Letters*, *31*(19), L19809. https://doi.org/10.1029/2004GL020875

Knipp, D., Kilcommons, L., Hairston, M., & Coley, W. R. (2021). Hemispheric asymmetries in Poynting flux derived from DMSP spacecraft. *Geophysical Research Letters*, *48*(17), e2021GL094781. https://doi.org/10.1029/2021GL094781

Lin, C. S., Sutton, E. K., Wang, W., Cai, X., Liu, G., Henney, C. J., & Cooke, D. L. (2022). Satellite in situ electron density observations of the midlatitude storm enhanced density on the noon meridional plane in the F region during the 20 November 2003 magnetic storm. *Journal of Geophysical Research: Space Physics*, *127*(5), e2021JA029831. https://doi.org/10.1029/2021JA029831

Liou, K., Newell, P. T., Sibeck, D. G., Meng, C., Brittnacher, M., & Parks, G. (2001). Observation of IMF and seasonal effects in the location of auroral substorm onset. *Journal of Geophysical Research*, *106*(A4), 5799–5810. https://doi.org/10.1029/2000JA003001

Liu, J., Wang, W., Burns, A., Liu, L., & McInerney, J. (2017). A TIEGCM numerical study of the source and evolution of ionospheric F-region tongues of ionization: Universal time and interplanetary magnetic field dependence. *Journal of Atmospheric and Solar-Terrestrial Physics*, *156*, 87–96. https://doi.org/10.1016/j.jastp.2017.03.005

Liu, J., Zhao, B., & Liu, L. (2010). Time delay and duration of ionospheric total electron content responses to geomagnetic disturbances. *Annals of Geophysics*, *28*(3), 795–805. https://doi.org/10.5194/angeo-28-795-2010

Lu, G., Goncharenko, L., Nicolls, M. J., Maute, A., Coster, A., & Paxton, L. J. (2012). Ionospheric and thermospheric variations associated with prompt penetration electric fields. *Journal of Geophysical Research: Space Physics*, *117*(8). https://doi.org/10.1029/2012JA017769

Lu, G., Hagan, M. E., Häusler, K., Doornbos, E., Bruinsma, S., Anderson, B. J., & Korth, H. (2014). Global ionospheric and thermospheric response to the 5 April 2010 geomagnetic storm: An integrated data-model investigation. *Journal of Geophysical Research: Space Physics*, *119*(12), 10375. https://doi.org/10.1002/2014JA020555

Lu, G., Richmond, A. D., Roble, R. G., & Emery, B. A. (2001). Coexistence of ionospheric positive and negative storm phases under northern winter conditions: A case study. *Journal of Geophysical Research*, *106*(A11), 24493–24504. https://doi.org/10.1029/2001JA000003

Mannucci, A. J., Tsurutani, B. T., Iijima, B. A., Komjathy, A., Saito, A., Gonzalez, W. D., et al. (2005). Dayside global ionospheric response to the major interplanetary events of October 29–30, 2003 "Halloween Storms". *Geophysical Research Letters*, *32*(12), L12S02. https://doi.org/10.1029/2004GL021467

Mannucci, A. J., Tsurutani, B. T., Kelley, M. C., Iijima, B. A., & Komjathy, A. (2009). Local time dependence of the prompt ionospheric response for the 7, 9, and 10 November 2004 superstorms. *Journal of Geophysical Research*, *114*(A10), A10308. https://doi.org/10.1029/2009JA014043

Maruyama, N., Richmond, A. D., Fuller-Rowell, T. J., Codrescu, M. V., Sazykin, S., Toffoletto, F. R., et al. (2005). Interaction between direct penetration and disturbance dynamo electric fields in the storm-time equatorial ionosphere. *Geophysical Research Letters*, *32*(17), 2–5. https://doi.org/10.1029/2005gl023763

Meier, R., Crowley, G., Strickland, D. J., Christensen, A. B., Paxton, L. J., Morrison, D., & Hackert, C. L. (2005). First look at the 20 November 2003 superstorm with TIMED/GUVI: Comparisons with a thermospheric global circulation model. *Journal of Geophysical Research*, *110*(A9), A09S41. https://doi.org/10.1029/2004JA010990

Meier, R. R. (2021). The thermospheric column O/N_2 ratio. *Journal of Geophysical Research: Space Physics*, *126*(3), e2020JA029059. https://doi.org/10.1029/2020JA029059

Mendillo, M. (2006). Storms in the ionosphere: Patterns and processes for total electron content. *Reviews of Geophysics*, *44*(4), 1–47. https://doi.org/10.1029/2005RG000193

Mendillo, M., Papagiannis, M. D., & Klobuchar, J. A. (1972). Average behavior of the midlatitude F-region parameters NT, Nmax and τ during geomagnetic storms. *Journal of Geophysical Research*, *77*(25), 4891–4895. https://doi.org/10.1029/JA077i025p04891

Oliveira, D. M., & Zesta, E. (2024). Interhemispheric energy input into the ionosphere-thermosphere system during magnetic storms: What we can and cannot learn from DMSP observations. *Journal of Geophysical Research: Space Physics*, *129*(5), e2024JA032486. https://doi.org/10.1029/2024JA032486

Pakhotin, I. P., Mann, I. R., Xie, K., Burchill, J. K., & Knudsen, D. J. (2021). Northern preference for terrestrial electromagnetic energy input from space weather. *Nature Communications*, *21*(199), 1–9. https://doi.org/10.1038/s41467-020-20450-3

Papitashvili, N. E., & King, J. H. (2020). OMNI 1-min Data [Dataset]. *NASA Space Physics Data Facility*. https://doi.org/10.48322/45bb-8792

Perlongo, N. J., & Ridley, A. J. (2016). Universal time effect in the response of the thermosphere to electric field changes. *Journal of Geophysical Research: Space Physics*, *121*(4), 3681–3698. https://doi.org/10.1002/2015JA021636

Prölss, G. (1993a). On explaining the local time variation of ionospheric storm effects. *Annales Geophysicae*, *11*, 1–9.

Prölss, G. W. (1993b). Common origin of positive ionospheric storms at middle latitudes and the geomagnetic activity effect at low latitudes. *Journal of Geophysical Research*, *98*(A4), 5981–5991. https://doi.org/10.1029/92JA02777

Qian, L., Burns, A. G., Solomon, S. C., Wang, W., & Zhang, Y. (2016). Solar cycle variations of thermospheric composition at the solstices. *Journal of Geophysical Research: Space Physics*, *121*(4), 3740–3749. https://doi.org/10.1002/2016JA022390

Qin, J., Liu, H., Yin, X., Liu, M., Wang, J., Mao, T., et al. (2023). Inferring the ionospheric state with the far ultraviolet imager on the Fengyun-4C geostationary satellite: Retrieval algorithm and verification. *Earth and Space Science*, *10*(12), e2023EA003222. https://doi.org/10.1029/2023EA003222

Qin, Y., Gu, S.-Y., Dang, T., & Dou, X. (2019). Ionospheric interhemispheric asymmetry induced by planetary wave under solar minimum condition. *Journal of Geophysical Research: Space Physics*, *124*(11), 9302–9314. https://doi.org/10.1029/2019JA026968

Richmond, A. D., & Roble, R. G. (1979). Dynamic effects of aurora generated gravity waves on the mid-latitude ionosphere. *Journal of Atmospheric and Terrestrial Physics*, *41*(7–8), 841–852. https://doi.org/10.1016/0021-9169(79)90127-2

Rideout, W., & Coster, A. (2006). Automated gps processing for global total electron content data. *GPS Solutions*, *10*(3), 219–228. https://doi.org/10.1007/s10291-006-0029-5

Ridley, A. J. (2007). Effects of seasonal changes in the ionospheric conductances on magnetospheric field-aligned currents. *Geophysical Research Letters*, *34*(5), L05101. https://doi.org/10.1029/2006GL028444

Ridley, A. J., Deng, Y., & Tóth, G. (2006). The global ionosphere–thermosphere model. *Journal of Atmospheric and Solar-Terrestrial Physics*, *68*(8), 839–864. https://doi.org/10.1016/j.jastp.2006.01.008

Ridley, A. J., Gombosi, T. I., & De Zeeuw, D. L. (2004). Ionospheric control of the magnetosphere: Conductance. *Annales Geophysicae*, *22*(2), 567–584. https://doi.org/10.5194/angeo-22-567-2004

Sazykin, S. (2000). *Theoretical studies of penetration of magnetospheric electric fields to the ionosphere* (Ph.D. thesis). Utah State University.

Schunk, R. W., & Nagy, A. F. (2000). *Ionospheres: Physics, plasma physics, and chemistry*. Cambridge University Press.

Strickland, D. J., Evans, J. S., & Paxton, L. J. (1995). Satellite remote sensing of thermospheric O/N2 and solar EUV.1.Theory. *Journal of Geophysical Research*, *100*(A7), 12217–12226. https://doi.org/10.1029/95JA00574

Sun, H., Hua, Z., Ren, J., Zou, S., Sun, Y., & Chen, Y. (2021). Matrix completion methods for the total electron content video reconstruction. *Annals of Applied Statistics*, *15*(3).

Sutton, E. K., Forbes, J. M., & Knipp, D. J. (2009). Rapid response of the thermosphere to variations in Joule heating. *Journal of Geophysical Research*, *114*(A4), A04319. https://doi.org/10.1029/2008JA013

Terefe, D. A., Nigussie, M., & Habarulema, J. B. (2024). The Effect of energy deposition hemispherical asymmetry on characteristics ofLSTIDs during 17 March 2015 geomagnetic storm. *Journal of Geophysical Research: Space Physics*, *129*(5), e2023JA031907. https://doi.org/10.1029/2023JA031907

Toffoletto, F., Sazykin, S., Spiro, R., & Wolf, R. (2003). Inner magnetospheric modeling with the Rice convection model. *Space Science Reviews*, *107*(1–2), 175–196. https://doi.org/10.1023/A:1025532008047

Tóth, G., Sokolov, I. V., Gombosi, T. I., Chesney, D. R., Clauer, C. R., De Zeeuw, D. L., et al. (2005). Space weather modeling framework: A newtool for the space science community. *Journal of Geophysical Research*, *110*(A12). https://doi.org/10.1029/2005JA011126

Tsurutani, B., Mannucci, A., Iijima, B., Abdu, M. A., Sobral, J. H. A., Gonzalez, W., et al. (2004). Global dayside ionospheric uplift and enhancement associated with interplanetary electric fields. *Journal of Geophysical Research*, *109*(A8), A08302. https://doi.org/10.1029/2003JA010342

Verkhoglyadova, O. P., Komjathy, A., Mannucci, A. J., Mlynczak, M., Hunt, L., & Paxton, L. J. (2017). Revisiting ionosphere-thermosphere responses to solar wind driving in superstorms of November 2003 and 2004. *Journal of Geophysical Research*, *122*(10). https://doi.org/10.1002/2017JA024542

Vierinen, J., Coster, A. J., Rideout, W. C., Erickson, P. J., & Norberg, J. (2016). Statistical framework for estimating GNSS bias. *Atmospheric Measurement Techniques*, *9*(3), 1303–1312. https://doi.org/10.5194/amt-9-1303-2016

Wang, X., Miao, J., Aa, E., Ren, T., Wang, Y., Liu, J., & Liu, S. (2020). Statistical analysis of Joule heating and thermosphere response during geomagnetic storms of different magnitudes. *Journal of Geophysical Research: Space Physics*, *125*(8), e2020JA027966. https://doi.org/10.1029/2020JA027966

Wang, Z., & Zou, S. (2022). COMPASS: A new COnductance model based on PFISR and SWARM satellite observations. *Space Weather*, *20*(2), e2021SW002958. https://doi.org/10.1029/2021SW002958

Wang, Z., Zou, S., Coppeans, T., Ren, J., Ridley, A., & Gombosi, T. (2019). Segmentation of SED by boundary flows associated with westward drifting partial ring current. *Geophysical Research Letters*, *46*(14), 7920–7928. https://doi.org/10.1029/2019GL084041

Wang, Z., Zou, S., Liu, L., Ren, J., & Aa, E. (2021). Hemispheric asymmetries in the mid-latitude ionosphere during the September 7–8, 2017 storm: Multiinstrument observations. *Journal of Geophysical Research: Space Physics*, *126*(4), e2020JA028829. https://doi.org/10.1029/2020JA028829

Weimer, D. R. (2005). Improved ionospheric electrodynamic models and application to calculating Joule heating rates. *Journal of Geophysical Research*, *110*(A5), A05306. https://doi.org/10.1029/2004JA010884

Wernik, A., Secan, J., & Fremouw, E. (2003). Ionospheric irregularities and scintillation. *Advances in Space Research*, *31*(4), 971–981. https://doi.org/10.1016/s0273-1177(02)00795-0

Wolf, R. A. (1983). The quasi-static (slow-flow) region of the magnetosphere. In R. L. Carovillano & J. M. Forbes (Eds.), *Solar Terrestrial Physics* (pp. 303–368). Springer.

World Data Center in Kyoto (2025). Retrieved from: https://wdc.kugi.kyoto-u.ac.jp/dstae/index.html

Workayehu, A. B., Vanhamki, H., & Aikio, A. T. (2020). Seasonal effect on hemispheric asymmetry in ionospheric horizontal and field aligned currents. *Journal of Geophysical Research: Space Physics*, *125*(10), e2020JA028051. https://doi.org/10.1029/2020JA028051

Yu, T., Cai, X., Ren, Z., Wang, Z., Pedatella, N. M., & Jin, Y. (2023). Investigation of interhemispheric asymmetry of the thermospheric composition observed by GOLD during the first strong geomagnetic storm in solar-cycle 25, 1: IMF by effects. *Journal of Geophysical Research: Space Physics*, *128*(10), e2023JA031429. https://doi.org/10.1029/2023JA031429

Yue, X., Wang, W., Lei, J., Burns, A., Zhang, Y., Wan, W., et al. (2016). Long-lasting negative ionospheric storm effects in low and middle latitudes during the recovery phase of the 17 March 2013 geomagnetic storm. *Journal of Geophysical Research: Space Physics*, *121*(9), 9234–9249. https://doi.org/10.1002/2016JA022984

Zhang, Y., Paxton, L. J., Morrison, D., Wolven, B., Kil, H., Meng, C. I., et al. (2004). O/N2 changes during1-4October 2002storms: IMAGE SI13andTIMED/GUVI observations. *Journal of Geophysical Research*, *109*(A10), A10308. https://doi.org/10.1029/2004JA010441

Zhu, Q., Lu, G., & Deng, Y. (2022). Low- and mid-latitude ionospheric response to the 2013 St. Patrick's day geomagnetic storm in the American sector: Global ionosphere thermosphere model simulation. *Frontiers in Astronomy and Space Sciences*, *9*, 916739. https://doi.org/10.3389/fspas.2022.916739

Zhu, Q., Lu, G., Lei, J., Deng, Y., Doornbos, E., van den Ijssel, J., & Siemes, C. (2023). Interhemispheric asymmetry of the thermospheric neutral density response to the 7–9 September 2017 geomagnetic storms. *Geophysical Research Letters*, *50*(11), e2023GL103208. https://doi.org/10.1029/2023GL103208

Zou, S., Moldwin, M. B., Ridley, A. J., Nicolls, M. J., Coster, A. J., Thomas, E. G., & Ruohoniemi, J. M. (2014). On the generation/decay of the storm enhanced density plumes: Role of the convection flow and field-aligned ion flow. *Journal of Geophysical Research: Space Physics*, *119*(10), 8543–8559. https://doi.org/10.1002/2014JA020408

Zou, S., & Ridley, A. J. (2016). Modeling of the evolution of storm-enhanced density (SED) plume during the Oct. 24-25, 2011 geomagnetic storm. In C. R. Chappell, R. W. Schunk, P. M. Banks, J. L. Burch, & R. M. Thorne (Eds.), *Magnetosphere-ionosphere coupling in the solar system*. John Wiley & Sons, Inc. https://doi.org/10.1002/9781119066880.ch16

Zou, S., Ridley, A. J., Moldwin, M. B., Nicolls, M. J., Coster, A. J., Thomas, E. G., & Ruohoniemi, J. M. (2013). Multi-instrument observations of SED during 24–25 October 2011 storm: Implications for SED formation processes. *Journal of Geophysical Research*, *118*(12), 7798–7809. https://doi.org/10.1002/2013JA018860